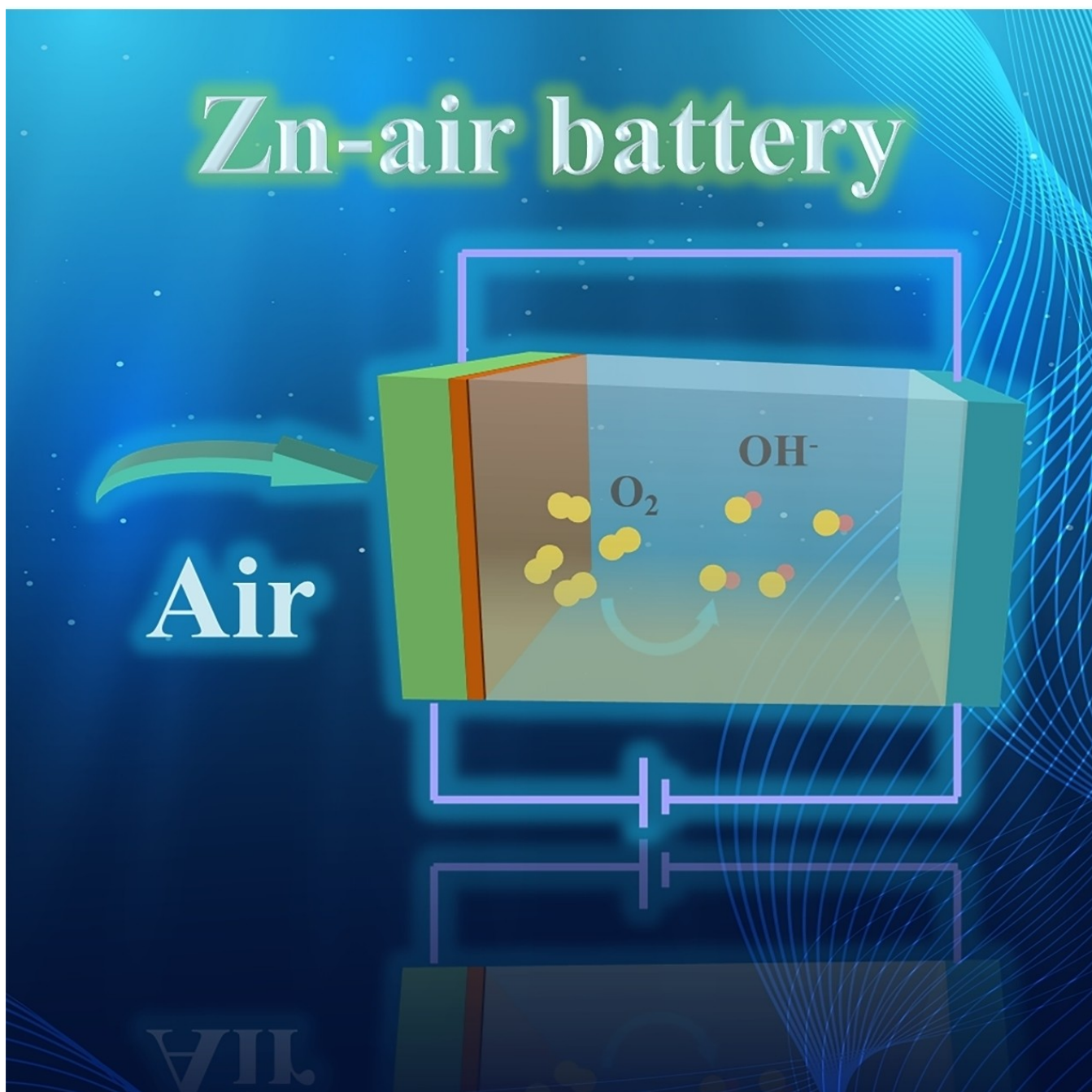




Metal-Organic Framework Materials as Bifunctional Electrocatalyst for Rechargeable Zn-Air Batteries

Fangqing Liu,^[a] Xiaoyi Lu,^[a] Chenglong Shi,^[a] and Zhipeng Sun^{*[a]}



Rechargeable Zn-air batteries offer the advantages of environmental friendliness, safety, low prices and high energy density, and are highly valued. However, the major challenge faced by rechargeable Zn-air batteries nowadays is the low energy efficiency due to the slow reaction kinetics of electrocatalyst at the air cathode. Bifunctional catalysts are key to the development of Zn-air batteries by improving their overall performance and long-term cycling stability. Metal-organic framework (MOF) materials have shown great benefits as oxygen electrocatalysts

in promoting oxygen reduction reaction (ORR) and oxygen evolution reaction (OER). This paper reviews the recent advances of three kinds of MOF materials as bifunctional catalysts for rechargeable Zn-air batteries. Additionally, this paper also discusses the synthetic design strategy of MOF composite derivatives, and concludes by suggesting the application of MOF materials in the field of rechargeable Zn-air batteries.

1. Introduction

In recent decades, the economy and society have been growing rapidly. The greenhouse effect produced by the excessive use of traditional fossil fuels has created serious environmental issues for the general public.^[1,2] While demanding higher economic levels, the demand for a sense of well-being in life is also gradually increasing. Countries worldwide are confronted with environmental challenges stemming from fossil energy consumption. The most important measure is to make great efforts to develop sustainable green energy. Solar, wind, water and tidal energy are all green energy sources, but not sustainable. They should be coupled with energy storage and conversion systems in order to stabilize storage and output for sustainability.^[3,4] Thus, research has been aimed at efficient energy storage and conversion systems.

With the advancement of technology, a plethora of devices have been developed for energy storage and conversion. Among these, metal-air batteries are considered promising candidates due to their high energy density and capacity.^[5,6] The metal-air battery comprises a metal anode, an electrolyte and an air cathode with various metals such as Li, Na, Fe, K, Mg, Al, and Zn being used as the anode material.^[7] Zinc-based metal-air batteries are preferred due to their favorable safety and environmental friendliness.^[8,9] Although button-type zinc air batteries were initially used in hearing aids. At the beginning of the 20th century, however, they faced challenges related to low efficiency and short lifespan which hindered large-scale commercialization.^[10] With the development of materials science, significant progress has been made in the study of gas diffusion electrodes, leading to a substantial enhancement in the power density of Zn-air batteries. In recent years, there have been continuous improvements in catalyst preparation technology and an increasing profound understanding of the underlying mechanism.^[11–13] Numerous studies have shown that the rechargeable Zn-air battery can undergo charge and discharge cycles by continuously performing oxygen reduction and precipitation at the air cathode. Yet, due to sluggish chemical reaction kinetics during charge/discharge process, particularly for oxygen reduction reaction (ORR) and oxygen evolution

reaction (OER), the energy efficiency of these batteries typically remains below 55–65%.^[14–17] Therefore, enhancing the reaction rate of oxygen on the air cathode stands as a crucial measure to improve energy conversion efficiency.

Currently, commercially available electrocatalysts for oxygen reduction and oxygen evolution at the air cathode include noble metals Pt/C and RuO₂, which exhibit fast reaction rates.^[18–21] However, these catalysts suffer from inherent drawbacks such as instability, short lifetimes, and high costs due to their precious metal composition. Consequently, researchers have directed their efforts towards developing non-precious metal electrocatalysts that offer enhanced stability, cost-effectiveness, and efficiency.^[22,23] Among the various research findings in this field, metal-organic framework materials have emerged as the most promising candidates.

Metal-organic skeletons (MOFs) formed by the coordination of metal ion centers with organic ligands are used as electrocatalysts because of the advantages of porous and high specific surface area.^[3,24] Porosity is an intrinsic feature of MOF, which is the result of the interactions between metal nodes and organic ligands to form an open framework, and is the most important advantage as an electrocatalyst.^[25–27] It is worth noting that the structural design of MOF materials is controllable, which allows the design of abundant active sites and ensures the high capacity of the materials. MOF and its derivatives are typical oxygen electrocatalysts not only based on their improved reaction rate, as well as high ionic diffusion capacity.

A considerable number of reviews comprehensively summarize the recent advancements in various types of unifunctional and bifunctional oxygen electrocatalysts.^[28–31] However, it is still imperative to review the progress of research on metal-organic framework (MOF) materials as oxygen electrocatalysts for rechargeable Zn-air batteries. This paper initially presents the structure and reaction mechanism of rechargeable Zn-air batteries. Subsequently, it illustrates the fundamental categories of MOF catalysts employed for rechargeable Zn-air batteries, including pristine MOFs, MOF derivatives, and composite derivatives (Figure 1). Furthermore, it provides an overview of synthetic strategies concerning the design of composite derivatives based on MOFs as oxygen electrocatalysts. Lastly, this article discusses the prospects of utilizing MOF catalysts for rechargeable Zn-air batteries.

[a] F. Liu, X. Lu, C. Shi, Z. Sun

School of Materials and Energy, Guangdong University of Technology,
Waihuan Xi Road, Guangzhou Higher Education Mega Center, Panyu
District, Guangzhou 510006, China
E-mail: zpsunxj@gudt.edu.cn

2. Overview of Rechargeable Zn-Air Batteries

The first zinc-air battery was created in 1878.^[32,33] The low performance of the battery limited its progress. Until 1977, primary Zn-air batteries were applied to hearing-aid. In latest decades, owing to the rapidly advancing lithium-ion batteries, Zn-air batteries have seen a declining research fervor. This is a result of the actual energy density of Zn-air batteries (< 200 Wh kg⁻¹) being much lower than that of lithium-ion batteries. Researchers believe that the large difference between the actual and theoretical energy densities of Zn-air batteries is mainly brought about by the hysteresis kinetics of the anode oxygen reduction and oxygen evolution reactions.^[34–37] As a consequence, Zn-air batteries have entered a low research period in the past. In the past few years, the theory of research in-depth, the reduction of lithium resources and the focus of the current society on energy issues, Zn-air batteries for its high open-circuit voltage, high power density, high safety advantages come back into the view of the general public.^[38,39] Following the evolution of science and technology, zinc-air batteries have moved from primary batteries to rechargeable batteries.

2.1. Constitution of Zn-Air Batteries

The structural components of a rechargeable Zn-air battery are illustrated in Figure 2. Similar to other metal-air batteries, it typically consists of a metallic anode, an electrolyte, and an air cathode.^[40,41] Among these constituents, the metallic anode is comprised of zinc flakes while the electrolyte predominantly comprises aqueous alkaline solutions. In terms of electrolyte selection, potassium hydroxide (KOH) solution is widely preferred due to its high electrical conductivity and rapid electron transfer capability as well as its cost-effectiveness.^[42] Alkaline conditions provide a more corrosion-resistant environment for

the metallic anode compared to acidic and neutral electrolytes. Although sodium hydroxide (NaOH) and lithium hydroxide (LiOH) can also serve as alkaline electrolytes, thicker KOH solutions exhibit higher ionic conductivity ($73.50 \Omega^{-1} \text{cm}^2 \text{ equiv}^{-1}$) along with lower viscosity, thereby facilitating mass-charge transport during cell reactions.^[43,44]

An air cathode comprises three components: a current collector, a gas diffusion layer, and an active catalyst layer. The collector typically consists of an electrically conductive metal, such as nickel foam. The gas diffusion layer acts as a conduit for oxygen transport and therefore necessitates the use of a hydrophobic material like polytetrafluoroethylene (PTFE).^[45] It prevents electrolyte leakage while ensuring optimal oxygen ingress into the battery system. The catalyst layer is a crucial element in the air cathode where it is widely acknowledged that the redox reaction of oxygen takes place at the three-phase interface (catalyst-electrolyte-oxygen). The catalyst surface plays an indispensable role, with the sluggish chemical process on the air cathode being identified as the primary factor impacting Zn-air batteries' performance due to its low electron transfer efficiency.^[46]

Flexible solid-state zinc-air batteries are also increasing as the demand for wearing electronic devices increases, and more and more work is coming out of the research reports. The major difference between liquid zinc air batteries and solid zinc air batteries is the electrolyte. The electrolyte in the liquid phase adds to the overall mass of the zinc-air battery and is slightly less safe compared to flexible zinc-air batteries. Currently, the using of polymer electrolytes greatly simplifies the design of zinc-air batteries and can be designed into a variety of battery shapes, making it easy to work with wearable electronic devices. The catalyst requirements for flexible solid-state zinc-air batteries, on the other hand, have not significantly changed compared to liquid zinc-air batteries. Both are highly relying on the catalyst on the air electrode, and the catalytic performance plays a key role in improving the battery performance.



Zhipeng Sun is a Distinguished Professor at the Guangdong University of Technology and Vice Dean of the School of Materials and Energy. He obtained his Ph.D. degree at Nanjing University of Aeronautics and Astronautics in 2010. He then held appointments at various universities, including the National University of Singapore, Nanyang Technological University, and Xinjiang University. His current research focuses on energy materials and catalysts.



Fangqing Liu received the Bachelor's degree in Chemistry from Lingnan Normal College in 2020 and the Master's degree in Materials and Chemical Engineering from Northwest Normal University in 2023. She is currently a Ph.D. candidate at the School of Materials and Energy, Guangdong University of Technology, and is supervised by Prof. Zhipeng Sun. Her current research is focused on zinc-air battery cathode catalysts.



Xiaoyi Lu is a graduate student pursuing a PhD with Prof. Zhipeng Sun, at the School of Materials and Energy, Guangdong University of Technology, China. Currently, she is focused on energy storage devices with special interest in potassium ion batteries. She is devoting herself to develop hard carbon anodes with excellent cycle life and satisfactory fast-charging ability.



Chenglong Shi received his Bachelor's degree in Chemical Engineering and Technology from the Huanghuai University in 2019 and Master's degree in Chemical Engineering from Guilin University of Technology in 2022. He is currently a Ph.D. candidate under the supervision of Prof. Zhipeng Sun at the School of Materials and Energy, Guangdong University of Technology. His current research is focused on NASICON cathodes of sodium ion battery.

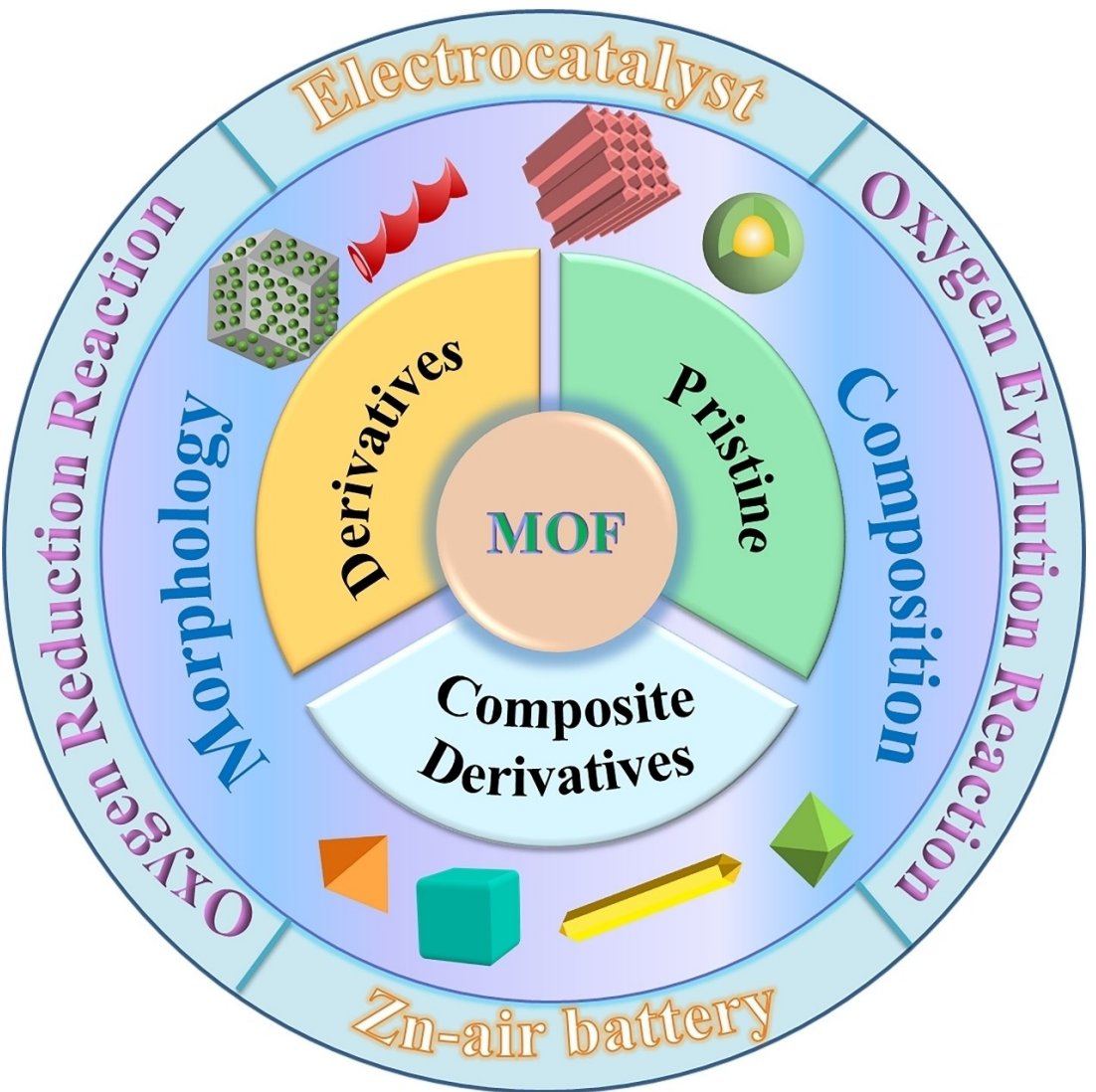


Figure 1. Metal-organic frame-based bifunctional electrocatalysts, including pristine MOFs, MOF derivatives and MOF composite derivatives.

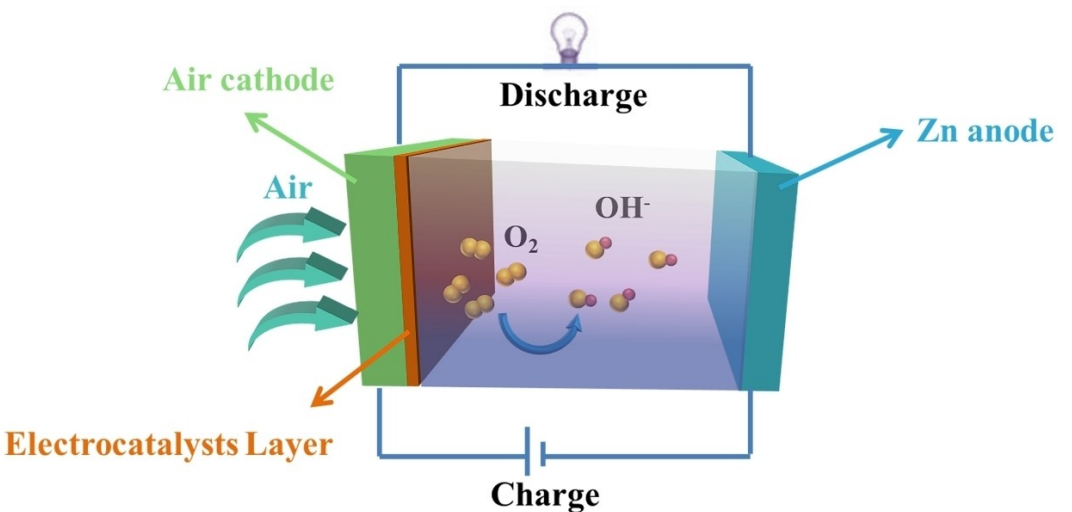


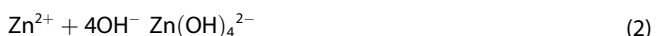
Figure 2. The structural of a rechargeable Zn-air battery.

2.2. Working Mechanization of Zn-Air Batteries

Rechargeable Zn-air batteries occur during charging and discharging in two main reaction processes: the ongoing dissolution of zinc flakes on the zinc negative electrode and the steady oxidation-reduction of oxygen on the air cathode. The reaction processes are explained in detail by reaction equations.

1. Zinc Electrode

The zinc electrode undergoes oxidation to form the zinc ion Zn^{2+} upon discharge, with the accompanying transfer of electrons through the electrolyte to the air electrode. Subsequently, Zn^{2+} reacts with OH^- in the electrolyte to generate soluble zincate species, namely $Zn(OH)_4^{2-}$.^[47] As the battery continues cycling over an extended period, there is a gradual accumulation of zincate ions leading to supersaturation and subsequent precipitation of zinc oxide on the surface of the zinc electrode. Simultaneously during charging, reduction of zincate ions occurs and they are deposited onto the surface of the zinc electrode. This process may potentially alter or modify the morphology of the zinc anode. The Equations (1)–(4) show the reaction process at the Zn electrode.



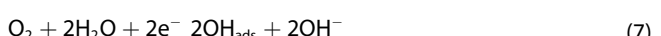
2. Air Electrode

Upon moving the electrons on the zinc sheet through the electrolyte to the air electrode, oxygen molecules in the air carry out an oxygen reduction reaction (ORR) at the electrode, leading to the production of OH^- . Afterwards, the OH^- produced on the air electrode travels into the electrolyte for freeing to the zinc electrode, making the conversion of Zn^{2+} into $Zn(OH)_4^{2-}$. This is the discharge on the air electrode. During charging, the overall phenomenon is inverted with the opposite process. Oxygen escapes from the air electrode in an oxygen evolution (OER) reaction. After the hydroxide loses electrons forming oxygen, the free electrons reduce the zincate ions. Equations (5) and (6) show the conversion process of oxygen.



In this case, the air electrode might appear in two ways during the charging and discharging of the battery for the oxygen reduction process: direct four-electron reaction pathway or indirect two-electron reaction pathway.

four-electron reaction:



two-electron reaction:



Reaction Equations (9) and (10) show that peroxides are created during the two-electron reaction. Breaking down the peroxides takes a long time and the substances produced from the peroxides are corrosive leading to premature degradation of the battery performance.^[48] Thus, the four-electron reaction with high energy efficiency is regarded as the optimal reaction pathway for oxygen reduction. It has been found through a large number of experiments that Pt follows the $4e^-$ reaction in the catalytic process and thereby exhibits better catalytic activity. Pt classified as a noble metal is expensive and has restricted reserves, both of which factors greatly restrict the widely usage of Pt catalysts.^[49]

Oxygen evolution is an opposite reaction of oxygen reduction, and the following are the possible reaction mechanisms of OER proposed by researchers. Most of them assume that the activity of the OER reaction is very essential linked to the ease of detachment of the reaction intermediates on the catalyst surface. The metal ions M form the intermediates MO, MOH, and MOOH, forming O_2 through the decomposition of MO or reacting with OH^- to form O_2 .



The free energy changes regarding each step of the OER are as follows. The overpotential is equivalent to the gap between the maximum free energy for each step of the reaction and the standard potential of 1.23 V. The maximum energy required for the reaction is the decisive step for the whole reaction process. The smaller the value of the difference between this step with 1.23 V, indicating that the reaction is easier to carry out and the catalytic performance is better.^[50,51]



It is noticed that IrO_2 and RuO_2 have excellent catalytic activity for OER but almost no effect on ORR, which are two

different reactions and difficult for one catalyst to satisfy both reactions at the same time. That is, an ideal air electrode catalyst needs to provide both ORR and OER catalytic activities. The key data for assessing ORR catalytic activity is the half-wave potential $E_{1/2}$ on the polarization curve. Positive half-wave potentials indicate higher ORR activity. The key index for evaluating the OER catalytic activity is the difference between the voltage at a certain current density (10 mA cm^{-2}) and 1.23 V, the overpotential. The more negative the overpotential, the better the OER activity. The two half-reactions compose the total reaction of the cell. The smaller the gap between the half-wave potential and the potential at 10 mA cm^{-2} , an indication of the superior properties of the cell.^[52] The current precious metals with better catalytic behavior are single-function catalysts with expensive prices. In terms of stability, precious metal catalysts are less stable and have poorer cycling ability when put together into batteries. All of these have been contributing factors in limiting practical applications.

The relationship between the free energies of intermediates during ORR and OER reactions has been reported to be represented by volcano diagrams. Each line stands for one step.^[53,54] When the adsorption energy of an intermediate varied, the energies of the other substances also varied. From the figure, it can be seen that the triangular region of ORR belongs to the oxygen reduction step of $\cdot\text{OH}$ and O_2 , while the OER region is the oxygen generation process of $\cdot\text{OH}$ and $\cdot\text{OOH}$. From the Figure 3, it can be observed that if the best ORR performance is required, the best OER performance cannot be satisfied, while if the best OER performance is achieved, the catalytic performance of ORR decreases accordingly.^[55] Therefore, there is a default assumption that when the region closer to the top of the volcano, the performance is better. Designing

a bifunctional catalyst is adjusted according to the volcano map.

The cathode is the spot where oxygen is reached and released, consequently it must have an effective surface area for gas transfer during gas diffusion. The gas diffusion electrode (GDE) is usually treated as an air electrode.^[56] With a high degree of porosity to evacuate the gas, it aims to achieve a rapid transfer of oxygen between electrolytes. In addition, oxygen needs to carry out a redox reaction, which means that rechargeable Zn-air batteries need to react at a voltage of 0.6–2 V and in a strongly alkaline electrolyte environment.^[57] This is a difficult condition for air electrodes. Hence air electrodes, especially the gas diffusion layer, should be more rationally designed. The surface of the air diffusion layer should also be hydrophobic to avoid electrolyte leakage and to enable air to enter the electrolytic cell in a stable manner. In order to increase the reaction rate of oxygen in the cell, one of the most important components of the air electrode is the catalyst layer. There is a three-phase reaction position between oxygen, electrolyte and catalyst, and in order for the three phases to be in balance, the surface of the catalyst needs to be hydrophilic.^[52] In conclusion, the bifunctional catalyst of the catalyst layer has the most significant impact on the performance of rechargeable zinc-air batteries. Accordingly, the development of bifunctional catalysts is one of the major efforts in the study of rechargeable zinc-air batteries. Among many research results, metal-organic framework materials are virtually one of typical catalyst materials.

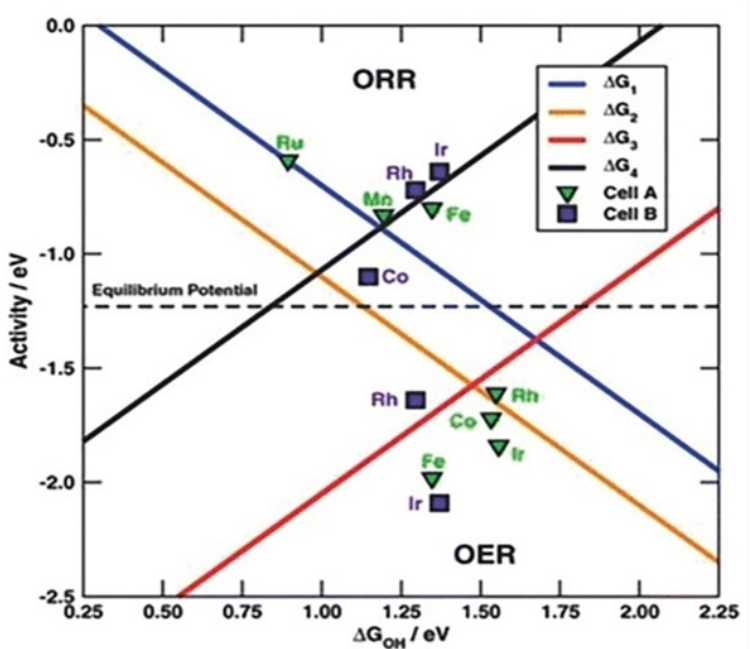


Figure 3. Volcano plots of ORR and OER.^[55]

3. Electrocatalysts of MOFs

Metal-organic framework materials, a group of crystalline materials consisting of metal ions or metal clusters bonded with organic ligands through coordination, are classical materials that have applications in drug-carrying, gas sensors, and energy conversion and storage in the last decade.^[58–60] Due to their satisfactory porous morphology and suitable functional groups, they are able to boost mass-charge transport in chemical reactions. The controllable high porosity as well as the large specific surface area provide an enabling basis for the study of oxygen electrocatalysts.^[61,62]

3.1. Pristine MOFs

Pristine MOFs are appealing candidates for electrocatalysis due to their tunable crystal porous structure and ordered arrangement of metal active sites. MOFs with transition metal nodes have been previously inducted with promising catalytic activity for electrocatalysis. However, highly active transition metal MOF bifunctional catalysts with fast kinetics capable of oxygen reduction and oxygen precipitation are still a great challenge. Researchers have designed modifications to enhance the catalytic activity of pristine MOFs from the inside and outside of the molecule.

Studies have discovered that the synergistic effect of bimetallic systems could decrease the energy boundary during ORR reaction and accelerate the reaction velocity. The addition of another metal to the pristine MOFs has reportedly been made to modify the internal structure of the MOFs to improve

the catalytic behavior. Figure 4 shows that Liu et al. designed transition metal MOF materials as highly active bifunctional oxygen electrocatalysts with lattice strain.^[63] The lattice-strained NiFe MOF exhibited an $E_{1/2}$ of 0.83 V on the ORR and an overpotential of 0.30 V on the OER. The catalytic activity of the material remained at about 97% from the initial activity after 200 h of continuous charge/discharge cycling under high current density. This suggests excellent stability and durability. The authors fabricated pristine NiFe MOF nanosheet arrays supported on Ni foam with 2,6-naphthalenedicarboxylic acid as a ligand using a low-temperature hydrothermal process. To synthesize lattice-strained NiFe MOF, the pristine NiFe MOF arrays were subjected to additional UV treatments at different radiation time ranges. After various numbers of UV treatments, the lattice-strained MOF interlayer distances varied, though the nanosheet arrays were morphologically intact. The lattice-strained NiFe MOFs experienced a fast and efficient 4e⁻ pathway in ORR and OER. Luis Echegoyen and others synthesized Co–Cu MOF structures based on 1,2,4,5 benzene tetramine (BTA) and benzene-1,3,5-tricarboxylic acid (BTC) with a low-temperature hydrothermal method.^[64] They varied the molar ratios of the two metal elements to modulate the structure of the MOFs, resulting in the modification of the catalytic property of the materials. The catalytic performance of the BTC–Co–O–Cu–BTA MOFs overcomes that of Pt/C, with onset and half-wave potentials of 1.06 V and 0.95 V/RHE, respectively. It is analyzed that the existence of a strong electronic coupling between the two metal elements (Co and Cu) with optimized inter-atomic electron transfer.

The electrocatalytic behaviors of the pristine MOF may be modulated via modifying the internal structure or components

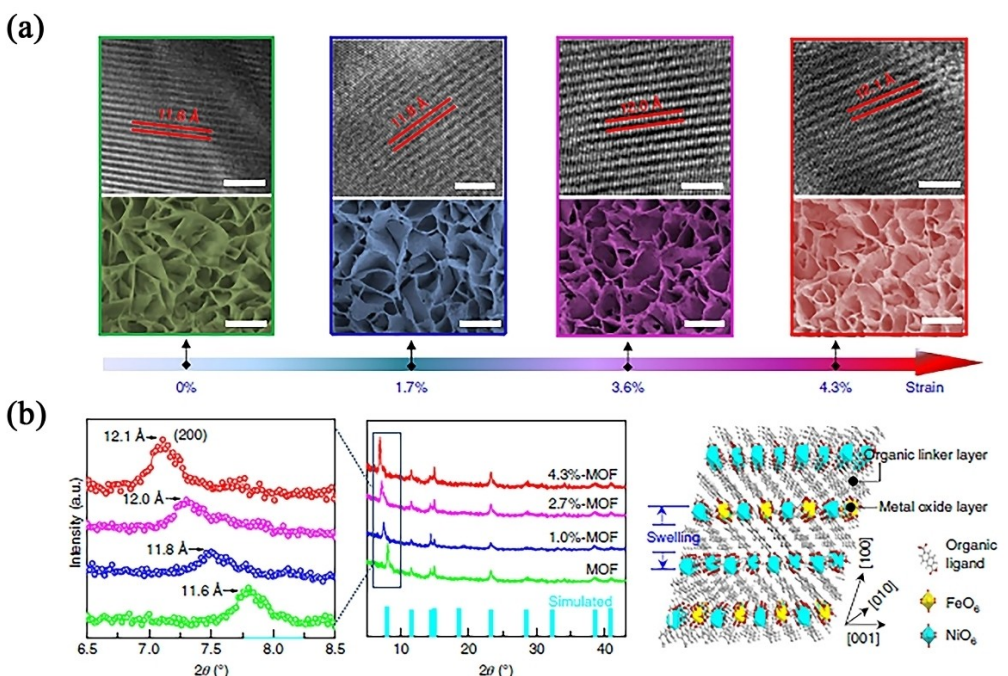


Figure 4. (a) HRTEM (top) and SEM (bottom) images of the pristine and lattice-strained MOFs. (b) Enlarged XRD and XRD patterns for them, and the XRD simulation of the NiFe MOF (turquoise bars). Schematic of the crystal structure variation of NiFe MOFs on ultraviolet irradiation.^[63]

of it. However, the electrical conductivity of the pristine MOF is still less than satisfactory with less than stable structure. According to the study, researchers proposed to prepare 2D MOFs to enlarge the surface area and expose more active sites, as well as to hybridize with conductive substrates to strengthen the electron transfer ratio. Zhong et al. *in situ* generated CoNi assistance of surfactant, which is showed by Figure 5.^[65] The rGO-coated uniformly distributed nanosheets displayed excellent electrocatalytic activity for OER and ORR. strong synergistic interaction between CoNi-MOF nanosheets and reduced graphene oxide was observed. The larger surface area of the 2D morphology exposes more active sites.^[66,67] The strong conductivity of reduced graphene oxide also offers promising conditions for the catalytic performance. The material is an excellent bifunctional electrocatalyst with high energy density and cycling stability in rechargeable Zn-air batteries.

Although a lot of pristine MOFs are employed for electrocatalysis, their bifunctionality still demands to be improved.^[27,68] In addition, the electrical conductivity and structural stability of the pristine MOFs should be promoted. The aforementioned weaknesses have restricted the further application of pristine MOFs in Zn-air batteries. Nowadays, exploring various materials

derived from MOF as catalysts for zinc-air batteries is more widespread.^[69]

3.2. MOF Derivatives

It was shown that most of the MOFs became a self-sacrificial template (Table 1).^[70–77] Some of the common MOFs materials include series, ZIF,^[69,78,79] MIL,^[80–82] and UIO,^[83] IRMOF,^[84]

3.2.1. MOF-Derived Metallic Compounds

MOF-derived transition metal compounds (e.g., transition metal oxides, metal sulfides, and metal phosphides) embedded in porous carbon matrices have attracted much attention due to the synergistic effect of the metal compounds with the porous carbon materials, resulting in significant improvement in the catalytic performance and durability.^[85–87] The MOF-derived transition metal oxides (Fe, Co, Ni, Mn, etc.) have received extensive attention as highly potential bifunctional electrocatalysts for ZABs. Firstly, the variable valence states and rich structures of transition metal oxides give them better oxidation-

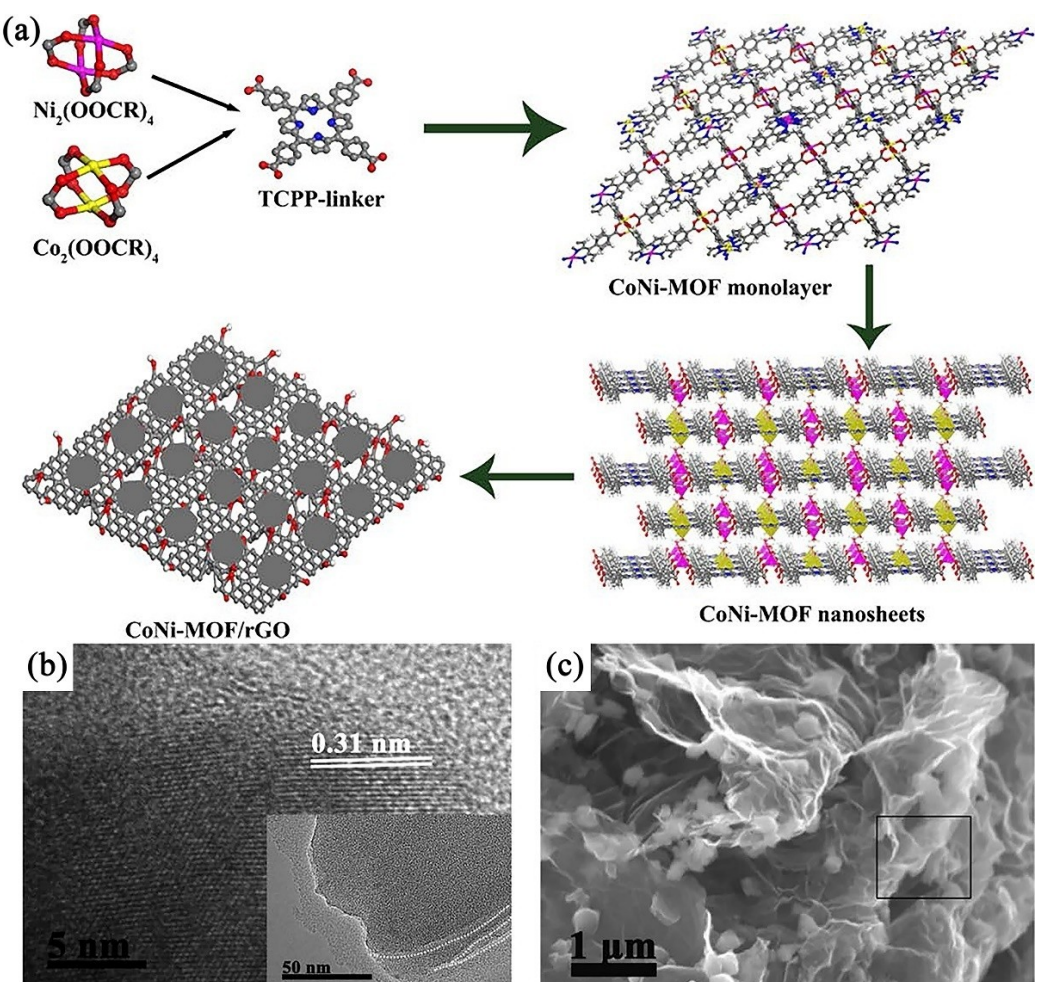


Figure 5. (a) The preparation of the CoNi-MOF/rGO catalyst. (b) TEM of CoNi-MOF nanosheets, and (c) SEM of CoNi-MOF/rGO.^[65]

Table 1. Electrochemical performance of MOF-based bifunctional catalysts.				
Electrocatalyst	MOF	ORR ($E_{1/2}$)/V	OER ($\eta = 10 \text{ mA cm}^{-2}$)/mV	Ref
Co/CoO@HNC	MIL-88A	0.83	430 (1 M KOH)	[70]
FeCo@CNTs-60	ZIF-67	0.95	530 (0.1 M KOH)	[71]
FeCo@NC-II	ZIF-L/ZIF-L	0.907	321 (1 M KOH)	[72]
CoFe/Fe3 C@CN-900	Fe-MOF	0.888	371 (1 M KOH)	[73]
Ni0.6Fe2.4O4@NC	NiFe-MOF	0.99	310 (0.1 M KOH)	[74]
Co _{SAs} @NC-920	ZnCo-ZIF@Zn-MOF-74	0.882	360 (0.1 M KOH)	[75]
CoFe-N-C	ZnCo-ZIF	0.90	440 (1 M KOH)	[76]
Co/Ce@NC	CoCe@ZIF-8	0.79	340 (1 M KOH)	[77]

reduction electrochemical properties. Secondly, the rich organic ligands in MOFs enable them to be uniformly dispersed in the porous carbon matrix in the process of controlled carbonization, which effectively improves the electrical conductivity and stability of the catalysts.^[88,89]

Cobalt oxides are currently the most popular among researchers.^[90–92] According to the study, it is well known that Co²⁺ catalysts contribute to the ORR performance, while it is the catalysts containing Co³⁺ that can contribute to the OER performance.^[93] Therefore, in order to obtain bifunctional

catalysts, researchers have introduced into the catalyst materials with Co₃O₄. Hu et al. (Figure 6(a)) prepared bifunctional catalysts by sandwiching Co/ZnCo₂O₄ nanoparticles intertwined with carbon nanotubes in leaf-shaped nitrogen-doped carbon microplates.^[94] Since the Co/ZnCo₂O₄@NC-CNTs catalyst exhibits a lot of metal-N_x and Co³⁺ active sites as well as interwoven carbon nanotubes on the surface of the carbon microplates, it shows excellent ORR/OER activity and a large power density of 305 mW cm⁻². Meanwhile, the catalyst is used in the application of flexible solid-state zinc-air batteries to demonstrate a high peak power density (151 mW cm⁻²). Efficient bifunctional catalysts were prepared by Tapas Kumar Maji et al (Figure 6(b)).^[95] The material was pyrolyzed from bimetallic MOF into oxide nanoparticles Ni_xCo_{1-x}@Ni_xCo_{1-x}O NPs and was encapsulated on n-doped carbon nanotubes (NCNTs) by calcination. Thermolysis of the bimetallic MOF resulted in stable growth of bimetallic nanoparticles on carbon nanotubes. Final calcination formed the core-shell structure. The catalyst showed an oxygen precipitation reaction overpotential of 380 mV at 10 mA cm⁻² current density and its onset potential of ORR is 0.87 V (vs. RHE) in alkaline medium. The material of this work was derivatized into a spinel structure by MOF. The synergistic interaction of two metals has shown long ago to be an effective way to raise the electrocatalytic activity.

In addition to Co-MOF, other metal-based MOF (e.g., Fe-based MOF) have also been chosen for designing the carbon encapsulated metal oxide materials act as efficient bifunctional electrocatalysts.^[96–98] Fe-based MOF with well-arranged morphologies were derived by tuning different metal sources and

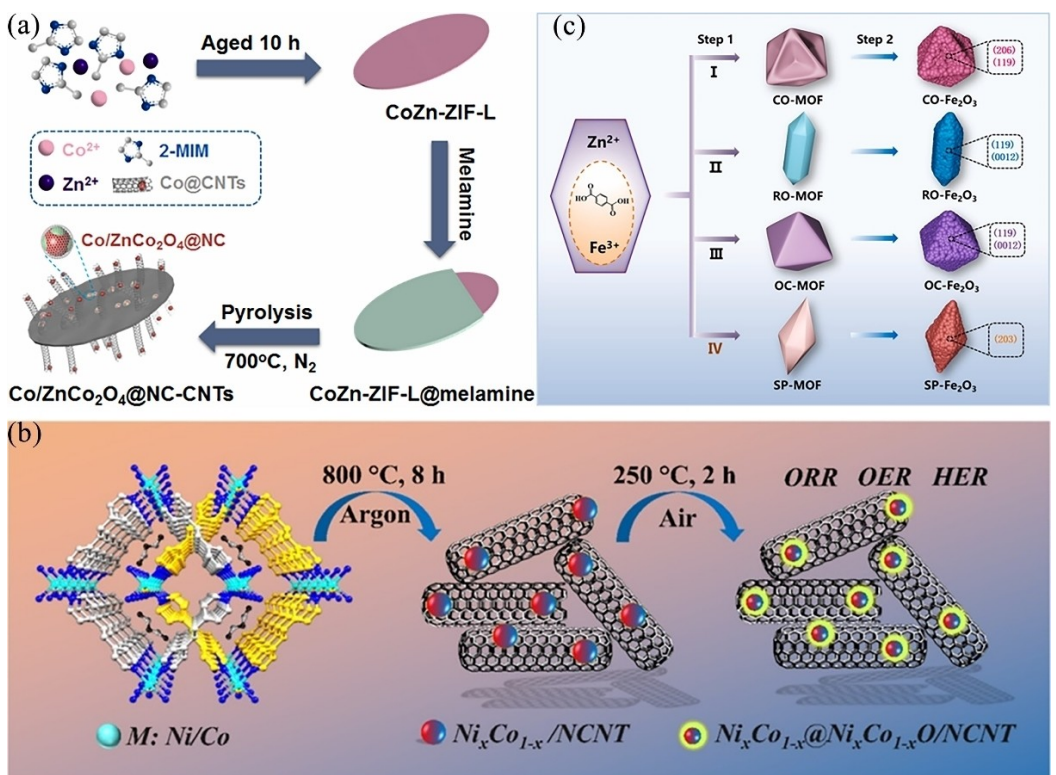


Figure 6. (a) The preparation of the electrocatalyst Co/ZnCo₂O₄@NC-CNTs.^[94] (b) Schematic Illustration of the Ni_xCo_{1-x}@Ni_xCo_{1-x}O/NCNT.^[95] (c) Diagrammatic representation of the synthesis procedure of Fe₂O₃ with different morphologies and structures.^[99]

ligands in different solvent fractions via a one-step solvothermal method by Bai et al (Figure 6(c)).^[99] Competition between ligand and solvent molecules as well as the metal sites was observed as a strategy to modulate the morphology of the MOF precursors. After pyrolysis, Fe_2O_3 was derived, and each morphology of the MOF exposed different active lattice planes, yielding different active sites. This work, utilized the competitive coordination reaction to modulate the morphology and active sites of MOF, and at the same time enhanced the ORR/OER properties of the material. Metal oxides are easily available and also offer superior catalytic activity. Because oxides suffer from the disadvantage of weak conductivity, they are commonly combined with conductive substrates to make stable, high-performance catalysts.^[14]

MOF-derived metal compounds also include transition metal sulfides, transition metal phosphides, transition metal nitrides, and others.^[100–102] Among them, transition metal sulfur compounds have received much attention for their diverse compositions, tunable electronic structures, unique redox properties, and multiple catalytic active sites.^[103] For example, CoS has been reported to be an efficient and stable electro-

catalytic active center based on carbon carriers.^[104] In Figure 7(a) and b), Li et al. reported a self-templating method to prepare $\text{CoS}_2@\text{MoS}_2@\text{NiS}_2$ nanopolyhedra with a double-shell structure and investigated their catalytic properties.^[103] The core-shell structure of ZIF-67@NiCo layered double hydroxide (NiCo LDH) has been prepared by the reaction of ZIF-67 with $\text{Ni}(\text{NO}_3)_2$. The double-shell layer $\text{CoS}_2@\text{MoS}_2@\text{NiS}_2$ was successfully prepared by further reaction of ZIF-67@NiCo LDH with Na_2MoO_4 and sequential sulfurization. In addition, $\text{CoS}_2@\text{MoS}_2@\text{NiS}_2$ can be assembled with not only rechargeable zinc-air batteries in addition to water decomposition devices. The excellent multifunctional catalytic performance can be contributed to the rational design of the multifunctional active centers, the strong electronic interactions between the active sites, and the special morphology structure. Transition metal sulfide (TMS) catalysts, especially Co-, Fe- and Ni-based sulfides, are frequently introduced into high-efficiency bifunctional electrocatalysts for rechargeable zinc-air batteries owing to their cost-effectiveness and ability to reduce overpotentials. Figure 7(c) displays that Ren et al. synthesized FeS_2 nanorods derived from Fe-MOF MIL-88 A with hollow double-shell structure and loaded with layered

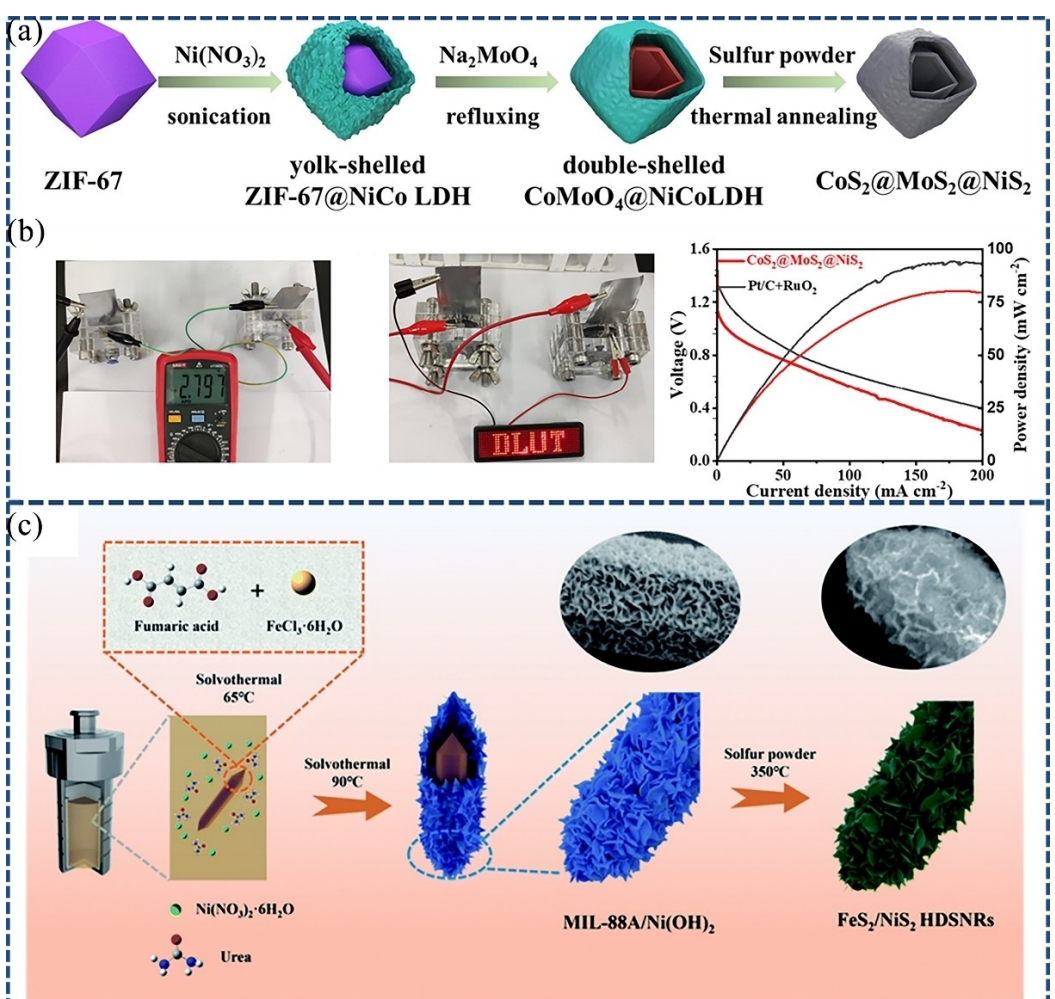


Figure 7. (a) The synthesis of $\text{CoS}_2@\text{MoS}_2@\text{NiS}_2$.^[103] (b) Open circuit voltage of two Zn-air batteries. The photograph of LED screen powered by them. Discharge polarization curves and corresponding power density of Zn-air batteries on the basis of $\text{CoS}_2@\text{MoS}_2@\text{NiS}_2$ and Pt/C + RuO₂.^[103] (c) Schematic illustration of the preparation of $\text{FeS}_2/\text{NiS}_2$ HDSNRs.^[105]

ultrathin NiS₂ nanosheets on the nanorods by hydrothermal self-templating method and solid-phase vulcanization strategy.^[105] The authors designed an appropriate solvent ratio (ethanol/water) in which the MOFs were etched and coprecipitated, forming the hollow double-shell structure. Due to the ingenious structural design and special electronic interactions at the inhomogeneous interface, the FeS₂/NiS₂ HDSNRs materials displayed better OER and ORR behaviors in alkaline solution than the single-component FeS₂ and NiS₂ materials. The catalyst as cathode of zinc-air batteries showed a peak power density of up to 130 mW cm⁻² at a current density of 5 mA cm⁻² and a high cycle life of up to 480 h. Transition metal sulfides/phosphides are reconfigured on the surface of the catalysts during the OER reaction process to produce highly active amorphous oxides/hydroxides, in which the actual active substances of OER are produced. NiS₂ and FeS₂ were shown in the literature to be the active sites of ORR, with the suggestion that the S–S single bond in S₂²⁻ plays the role of the catalytic active center. Despite excellent catalytic activity, transition metal sulfides are highly unstable and are oxidized to oxides or hydroxides during OER reactions. Therefore, it is necessary to use the transition metal sulfides as electrocatalysts combined with more *in situ* analyses to determine the true active component.

Zhang et al. constructed hierarchical core-shell ORR catalysts (Co₂N/CoP@PNCNTs) by embedding cobalt phosphide and cobalt nitride into N- and p-doped carbon nanotubes (PNCNTs) through carbonizing, nitriding and phosphorylating Co-MOF precursors.^[106] The material exhibited excellent electrocatalytic activity in alkaline solution with a half-wave potential of 0.85 V. The Zn-air battery assembled from Co₂N/CoP@PNCNTs served as an air cathode with a specific capacity of 823.8 mAh kg⁻¹. Due to the synergistic interaction between Co₂N/CoP and mesoporous N- and p-doped carbon nanotubes, the catalytic performance and stability of Co₂N/CoP@PNCNTs are outstanding. Metal phosphides are typically complexed with other efficient ORR catalysts to achieve bifunctional catalysts, such as metal nitrides.^[107] MOF-derived metal nitrides are formed by calcination of MOF containing nitrogen-containing organic ligands combined with transition metals. MOFs can directly derivatize into metal nitrides by itself and provide a direct carbon support for the metal nitrides, which easily obtains highly active ORR catalysts. However, the ligand number between N and metal is difficult to define, and the weak crystallinity of metal nitrides needs to be determined by more in-depth analytical methods.^[108]

3.2.2. MOF-Derived Metal Alloy Materials

The results demonstrate that the alloy structure can modulate the adsorption energy of transition metals on O₂, thereby enhancing the electrocatalytic performance of both ORR and OER. The utilization of small-sized active metal nanoparticles and their ability to reduce surface energy contribute to increased electrocatalytic activity in nanomaterials. Currently, bimetallic alloys derived from MOFs are typically prepared

through direct carbonization of bimetallic MOF precursors. Lei et al. (Figure 8(a)) employed a template-assisted method to synthesize small-sized Fe-ZIF crystals *in situ* on hollow poly-pyrrole spheres (h-PPy).^[109] This resulted in uniform dispersion of ultrafine CoFe nano-alloys on N-doped hollow carbon microspheres, leading to high ORR activity. CoFe/N-HCS also exhibited a low overpotential of 292 mV for OER at 10 mA cm⁻², demonstrating its superior bifunctional catalytic properties. Furthermore, CoFe/N-HCS was successfully applied in liquid zinc-air batteries with improved energy density (882.3 Wh kg_{Zn}⁻¹) and cycling stability. Zheng et al., on the other hand, synthesized Ni₃Fe nano-alloy electrocatalysts by hybridizing Ni-MOF with Fe, followed by mixing it with melamine and pyrolyzing the mixture (Figure 8(b)).^[110] Nitrogen-doped carbon nanotubes were used as packaging material for the Ni₃Fe alloy nanoparticles. The synergistic effect between the MOF precursor and melamine prevented agglomeration of metal particles due to framework restrictions imposed by the MOF structure. Ni₃Fe-NCNTs-800 exhibited excellent electrochemical catalytic performance with half-wave potential for ORR at 0.862 V and overpotential for OER at 353 mV@10 mA cm⁻², resulting in a potential gap of 0.72 V. The authors established that the strong coupling present in the Ni₃Fe bimetallic reaction process reduces the reaction potential barrier by density flooding theory (DFT) calculations. In addition, the liquid zinc-air battery assembled with Ni₃Fe-NCNTs-800 as the air cathode catalyst exhibited an ultra-high peak power density (211 mW cm⁻² at 240 mA cm⁻²), specific cell capacity (806 mAh g_{Zn}⁻¹), and excellent cycling stability (1,350 cycles).

Studies have demonstrated that the support of alloy catalysts is very significant for the catalytic performance. Employing graphitic carbon encapsulated alloy nanoparticles is a really encouraging strategy to ensure long lasting durability and increase catalytic activity. A bamboo-like nitrogen-doped carbon nanotube packed Co_{0.25}Ni_{0.75} alloy electrocatalyst (Co_{0.25}Ni_{0.75}@NCNT) was synthesized by C. Retna Raj et al.^[111] The authors used a one-step thermal reduction method with dicyandiamide and NiCo-MOF precursors to prepare the material. The hollow NiCo-MOF acted as a self-sacrificial template, providing a suitable growth environment to the controlled growth of Co_{0.25}Ni_{0.75} alloy and nitrogen-doped carbon nanotubes. The synergistic interaction between Co_{0.25}Ni_{0.75} alloy and nitrogen-doped carbon nanotubes strengthened the bifunctional activity and excellent durability of the composites. A Zn-air aqueous solution battery was prepared with Co_{0.25}Ni_{0.75}@NCNT-based air cathode. The cell was characterized by a maximum peak power density of 167 mW cm⁻². Fe_{0.18}Co_{0.82} alloy particles anchored on nitrogen-doped porous carbon hollow spheres (Fe_xCo_{1-x}/N-C) with spray pyrolysis (SP) technique was employed by Wang et al.^[112] The metal oxides obtained from spray pyrolysis system and the zinc species in the metal-organic skeleton were volatilized at high temperatures, forming a hierarchical porous structure and exposing the FeCo nanoparticles on the carbon substrate to full exposure. This work led to the evaporation of Zn species from ZIF-8 during subsequent pyrolysis, and this resulted in the formation of a porous carbon structure with a high specific

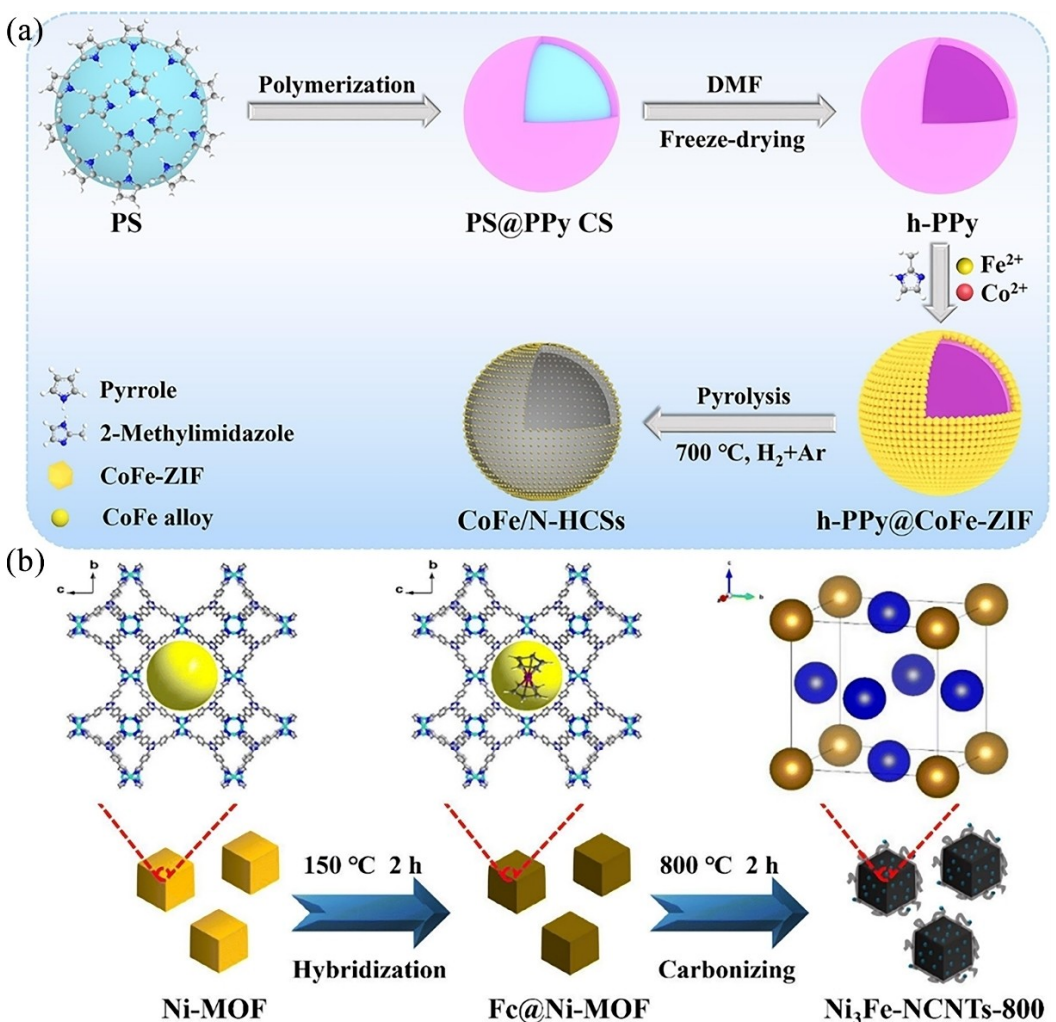


Figure 8. (a) Illustration of the synthesis of CoFe/N-HCSs.^[109] (b) Schematic diagram of the preparation process of Ni₃Fe-NCNTs-800.^[110]

surface area. Accordingly, in order to achieve superior stability in oxygen electrocatalysis, FeCo alloys with precisely controlled stoichiometric ratios were incorporated into nitrogen-doped porous carbon. The interaction among Fe and Co created electronic active configurations that formed the phenomenon of electronically rich states on the graphene surface, which improved the electrical charge distribution of the graphene layer, thereby enhancing the catalytic performance. Figure 9(a) displays the constructed metal-loaded N-doped defective carbon patterns of Fe_{0.2}Co_{0.8}/N-C and Co/N-C. The incorporation of Fe decreases the overpotential of the decisive velocity step, as calculated by DFT. In addition, the metal- N_x that was formed by the combination of N in the MOF and metal (Fe/Co) can also be served as an ORR active site. Within this structure, the Fe_{0.18}Co_{0.82} alloy and binary metal active sites (Fe-N_x/Co-N_x) deliver superior ORR half-wave potentials ($E_{1/2} = 0.84$ V), which are better than 20% Pt/C, and exhibit lower overpotentials (280 mV) than RuO₂ in the OER (Figure 9(b)). The alloy materials are more promoted for oxygen electrocatalysis in combination with other active materials.

3.3. MOF-Derived Carbon Materials—M–N–C

Metal-nitrogen-carbon (M–N–C) materials have been widely reported in recent years. DFT calculations have shown that the M–N₄ sites are active for oxygen adsorption and O–O bond breaking during the ORR process, which is the same as the noble metal Pt.^[113–115] MOF-derived M–N–C materials, consisting of carbonized ligand frameworks and abundant transition metal sites, were found to exhibit excellent ORR activity and OER performance. Therefore, it has drawn wide attention in catalysis.^[116–118]

In Figure 10(a and b), Sung Jong Yoo's group reported a Co-ZnO–C complex by melamine encapsulation with zeolite imidazole framework (ZIF-8) as precursor and template.^[119] This preparation strategy led to the formation of Co–N–C that formed meso- and macroporous hierarchical structures while maintaining microporosity. The stability of Co–N–C catalysts was confirmed to be superior to that of other M–N–C catalysts (M=Fe, Ni, Cr, and Mn) by density functional theory analysis. In addition, it is revealed that the interaction between Co–N₄ and organic compounds enhances the oxygenophilicity, which

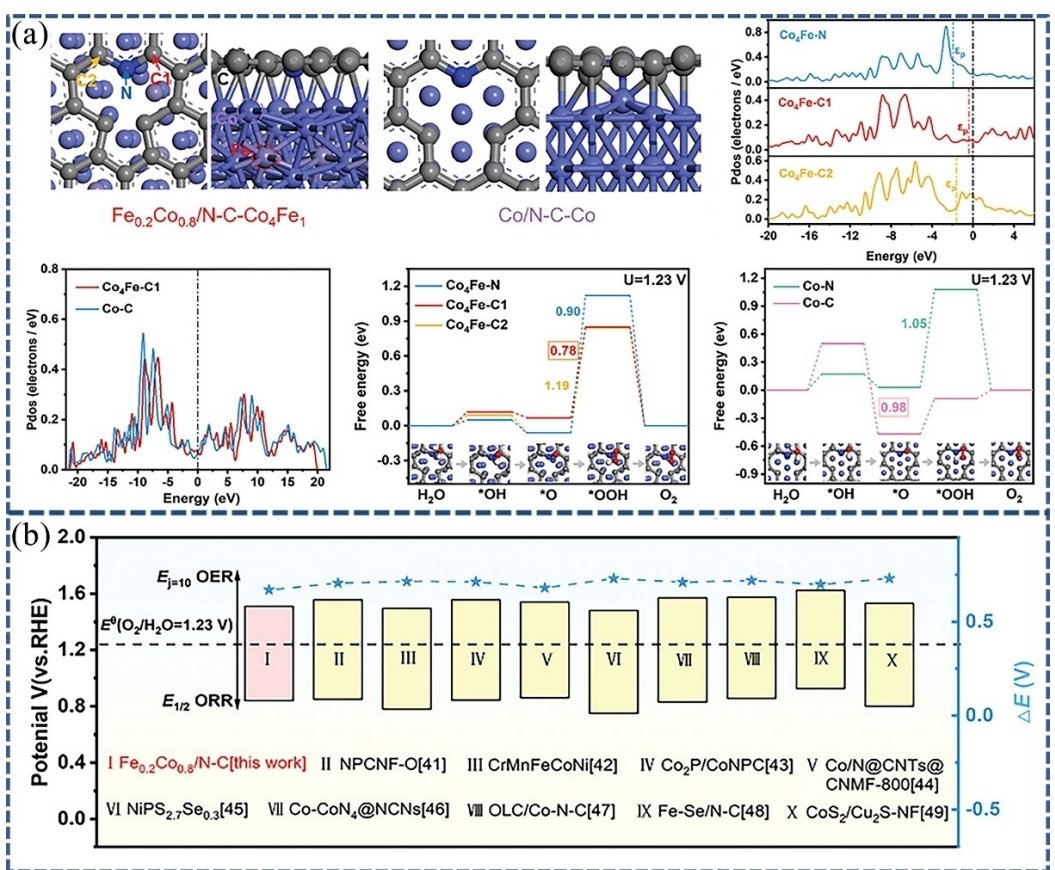


Figure 9. (a) Top and side views of the optimized geometry models for $\text{Fe}_{0.2}\text{Co}_{0.8}/\text{N-C}$ and $\text{Co}/\text{N-C}$ (N, C1, and C2 are the adsorption sites); The PDOS of N and C atoms in $\text{Fe}_{0.2}\text{Co}_{0.8}/\text{N-C}$ and $\text{Co}/\text{N-C}$ catalysts; Free energy diagram of the OER process for them at the equilibrium potentials of $U=1.23\text{ V}$. (b) A Comparison of the efficiency of a non-noble metal bifunctional electrocatalyst with $\text{Fe}_{0.2}\text{Co}_{0.8}/\text{N-C}$.^[112]

promotes the $4e^-$ ORR activity (Figure 10(a)). The unique structure of the catalyst shows its superior durability in actual equipment operation and stability analysis. Wang et al. synthesized carbon vacancy modified Fe-N-C SACs ($\text{Fe}_H\text{-N-C}$) by controlling the chemical environment around M-N_4 (Figure 10(c)).^[120] In this work, an engineered defects, electronic structure optimization strategy were applied. A half-wave potential ($E_{1/2}$) of 0.91 V and a durability of 100,000 cycles were observed for the $\text{Fe}_H\text{-N-C}$ catalyst. Density functional theory (DFT) calculations in Figure 10(d) verified that the carbon vacancies around the metal N_4 sites reduced the adsorption free kinetic of OH^* , slowed down the metal dissolution rate, and significantly improved the ORR reaction kinetics and stabilization. Therefore, $\text{Fe}_H\text{-N-C}$ SACs have high power density and long-term stability over 1200 h in rechargeable zinc-air batteries (ZABs). Zhang et al. reported a method for the preparation of microporous N-doped carbon electrocatalysts enriched with FeN_4 sites assisted by NaCl .^[121] Calcination of a mixture of ZIF-8 and NaCl yielded a porous N-doped carbon material (NC-NaCl). A second stage of pyrolysis was carried out after attaching iron ions (Fe^{3+}) to NC-NaCl to obtain porous Fe/NC-NaCl electrocatalysts. The porous surface provided by ZIF-8 and NaCl allowed for a more uniform dispersion of FeN_4 sites

and a greater density ($26.3 \times 10^{19}\text{ sites g}^{-1}$). The exposed FeN_4 are beneficial for the ORR process because they are easy to adsorb and reduce O_2 .

3.4. MOF Composite Derivatives

It is well known that pristine MOFs has the disadvantage of poor electrical conductivity, thus most researchers combine MOFs with conductive materials. This is expected to further strengthen the electronic conductivity and catalytic capability of Zn-air batteries. Recent studies have illustrated that pairing different types of MOFs with each other can lead to different effects, which not only regulate the formation of various morphologies as well as the catalytic properties.^[49]

Fe/N/P tri-doped carbon nanotubes (P-Fe-N-CNTs) electrocatalysts enriched with porous structure were prepared from the mixed phosphorylation pyrolysis of ZIF-8 and MIL-101 by Yi et al.^[122] ZIF-8 was used as the N-C precursor. In particular, Zn species evaporated at about 900°C , forming many pores, which increased the specific surface area of the material and thus facilitated gas diffusion. The authors promoted the formation of swollen P-Fe-N-CNTs catalysts using NaH_2PO_2 as a P source and

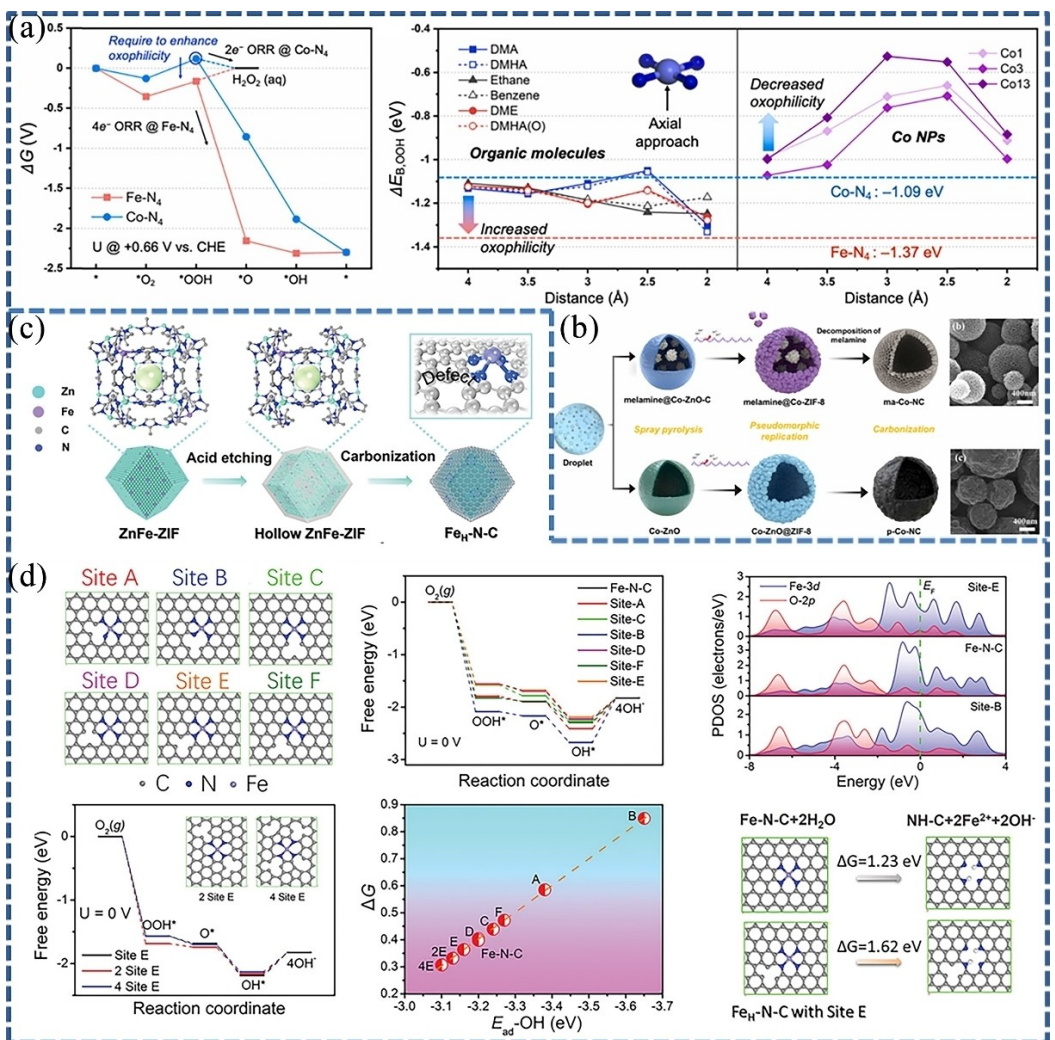


Figure 10. (a) Calculated free energy profile of associative ORR pathway for bare Co-N_4 and Fe-N_4 active sites. Effect of axial-coordination on $^*\text{OOH}$ binding strength according to chemical species and distances.^[119] (b) Schematic for synthesis of ma-Co-NC (melamine add ed Co-NC) and p-Co-NC .^[120] (c) Schematic illustration of synthesis procedure for FeH-N-C catalysts.^[121] (d) The vacancy effects in TM-N-C structures for ORR.^[119]

reducing agent, while accelerating the conversion of Fe in MIL-101, which catalyzed the in-situ growth of carbon nanotubes. The DFT findings also confirmed that appropriate p-doped carbon nanotubes could weaken O^* , which implied that P could change the electronic structures (Figure 11(a)). The rational design of interfacial structures has emerged as one of the most effective strategies to improve the efficiency, selectivity and stability of ORR and OER electrocatalysis. Interfacial engineering not only allows the fabrication of different structures to accelerate interfacial charge transfer between neighboring regions, but also the formation of enriched defects to improve electrocatalytic performance. The concept of interfacial engineering was proposed by Hu et al. for the preparation of N-doped carbon nanoboxes constrained by Co/MoC nanoparticles (Figure 11(b)).^[123] The authors constructed multifunctional electrocatalysts with uniform ZIF nanocubes as precursors, which were coated with polydopamine-molybdenum layers and then pyrolyzed. The Co@IC/MoC@PC catalysts exhibited excellent electrochemical ORR property with a

positive $E_{1/2}$ of 0.875 V. The materials were applied in zinc-air batteries to obtain a specific capacity of 728 mAh/g, a high open-circuit voltage of 1.482 V and a low charge/discharge voltage gap of 0.41 V.

4. Synthesis and Regulating Strategy of MOF Composite Derivatives for ORR/OER

4.1. Morphological Design of Composites Based on MOF Derivatives

The proper design of the morphology provides a more favorable location for accelerating the ORR and OER reactions. In order to promote the oxygen electrocatalytic reaction, the morphology is required to be designed to expose more active sites and at the same time to achieve fast mass transfer.

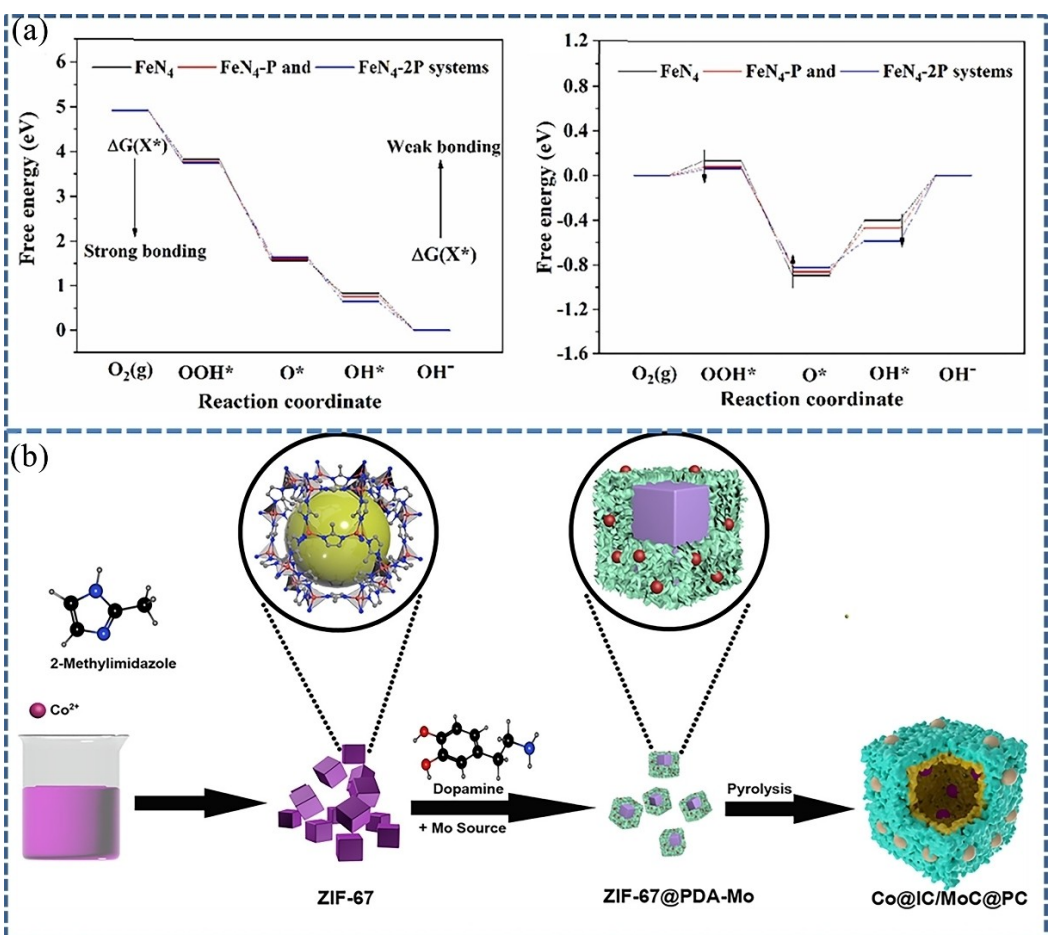


Figure 11. (a) Free energy diagram of the Fe-N-C and P-doped Fe-N-C systems at 0.00 V and 1.23 V.^[122] (b) Preparation Path for the Co@IC/MoC@PC product.^[123]

Therefore, the morphology of MOF-derived composites is a very essential step in the program design.

The optimized design of the morphology facilitates a more favorable location for enhancing the ORR and OER reactions. To promote the oxygen electrocatalytic reaction, it is crucial to tailor the morphology in order to expose a greater number of active sites while ensuring efficient mass transfer. Therefore, meticulous control over the morphology of MOF-derived composites plays a pivotal role in program design. Typically, morphological engineering is conducted on precursors, taking advantage of the inherent structural stability of MOFs which allows for partial retention of their morphology under appropriate carbonization conditions. Generally, MOFs serve as sacrificial templates wherein various types can be selected or other materials can be compounded onto them with altered compounding conditions to yield diverse morphologies. For example, polyhedra, nanorods, nanospheres, nanosheets, nanowires, and some three-dimensional layered structures are all advantageous morphologies for catalysts. Xiongwen Lou's group studies MOFs materials in the form of polyhedra, nanoboxes, nanocages,^[124] nanosheets, hollow nanoboxes, and yolk-shell structures. The authors used bimetallic-organic frameworks (Mn-MIL-100) as precursors to derive into abundant

MnO/Co heterointerfaces on the polyhedral carbon skeleton formed with MOFs.^[125] In order to maintain the octahedral morphology of the MILs, a thermogravimetric analysis was done prior to carbonization to ensure their complete decomposition to obtain highly crystalline carbon materials with high degree of graphitization (Figure 12(a)). In this way, more oxygen vacancies are derived to raise the catalytic capacity. The authors' team also designed NiMn-MOF nanosheet catalysts to promote oxygen electrocatalysis. They reported a method to grow layered NiMn-MOF nanosheets on multichannel carbon fibers (Figure 12(b and c)).^[126] The synergistic effect between Ni and Mn nodes in the nanosheets yielded superior ORR ($E_{1/2} = 0.85$ V) and OER ($\eta = 280$ mV@10 mA cm⁻²) performance. Through DFT calculations, it is revealed that the strong coupling interactions between neighboring Ni and Mn nodes favor the generation of key *O and *OOH intermediates in the ORR and OER processes.

To enhance the specific surface area of catalysts and facilitate mass transfer, hollow-structured MOFs have emerged as a prominent research focus. Hollow-structured materials exhibit high specific surface-to-volume ratios and low densities, rendering them ideal for micro-scale reactions. Their increased loading capacity effectively reduces the distance required for

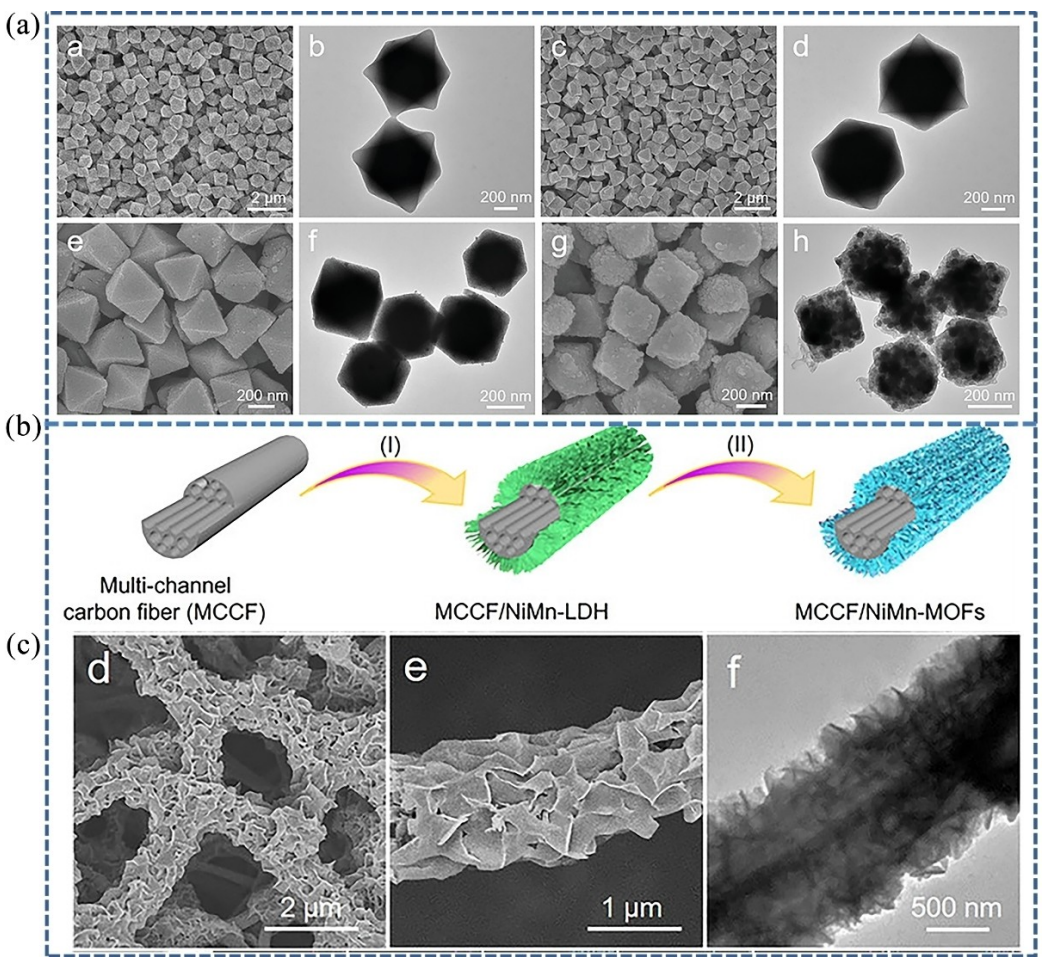


Figure 12. (a) FESEM and TEM images of Mn-MIL-100, Co/Mn-MIL-100, MnO/PAC, and MnO/Co/PGC.^[125] (b) Image of the preparation method of MCCF/NiMn-MOFs.^[126] (c) FESEM images, TEM image of MCCF/NiMn-MOFs.^[126]

mass-charge transfer. Consequently, hollow structures have garnered significant attention in various applications including electrochemical energy storage, electrocatalysis, and sensing technology. There are various synthetic methods to prepare hollow MOFs composites: template-mediated assembly, step-wise dissolution-regeneration, selective chemical etching, interfacial ion exchange, heterophase contraction and autocatalytic pyrolysis.^[127] Among these selective etching, phenolic acids (tannic acid, gallic acid) are generally available as etching reagents. Hollow MOFs superstructures can be formed by leaving them in phenolic acid for a few minutes.^[128] The shape and size of the original non-hollow structure is maintained during the etching process because the surface region of the MOFs is protected by the metal-phenolite network formation and the free protons released from the phenolic acid dissolve the interior of the MOFs backbone. As shown in Figure 13(a), Guo et al. used microwave-assisted synthesis of multilayered CuO@NiO hollow spheres.^[129] Owing to the different ion exchange rates from the outer shell to the core, the content of Cu decreases from the outside to the inside and the content of Ni increases. The unique multilayer structure improves the electron storage performance.

The template method is the most commonly employed technique for preparing hollow MOFs. Suitable MOFs are provided as self-sacrificial templates along with precursors of the desired material. Upon removal of the template, the precursor undergoes transformation into the final product. The process of compositing involves considering surface ligand-induced assembly and electrostatic interactions, specifically how to effectively combine the precursor and template while utilizing functional groups to modify the template. The monoporous cobalt/nitrogen-doped carbon hollow particles studied by Xiongwen Lou's group not only exhibit excellent bioproperties, but also high activity and excellent durability.^[130] A facile synthesis method was employed to prepare monoporous cobalt/nitrogen-doped carbon (Co/NC) hollow particles, which exhibited excellent electrocatalytic activity towards oxygen reduction reaction (ORR) (Figure 13(b)). In contrast to previous studies, a uniform layer of ZIF-67 particles was initially grown on polystyrene (PS) spheres to form PS@ZIF-67 composite particles as precursors. Subsequently, these precursors were converted into hollow particles with large through-holes on the surface through a carbonization process. The incorporation of PS spheres in the MOFs composite precursor served as a template for thermal degradation. The formation of holes on

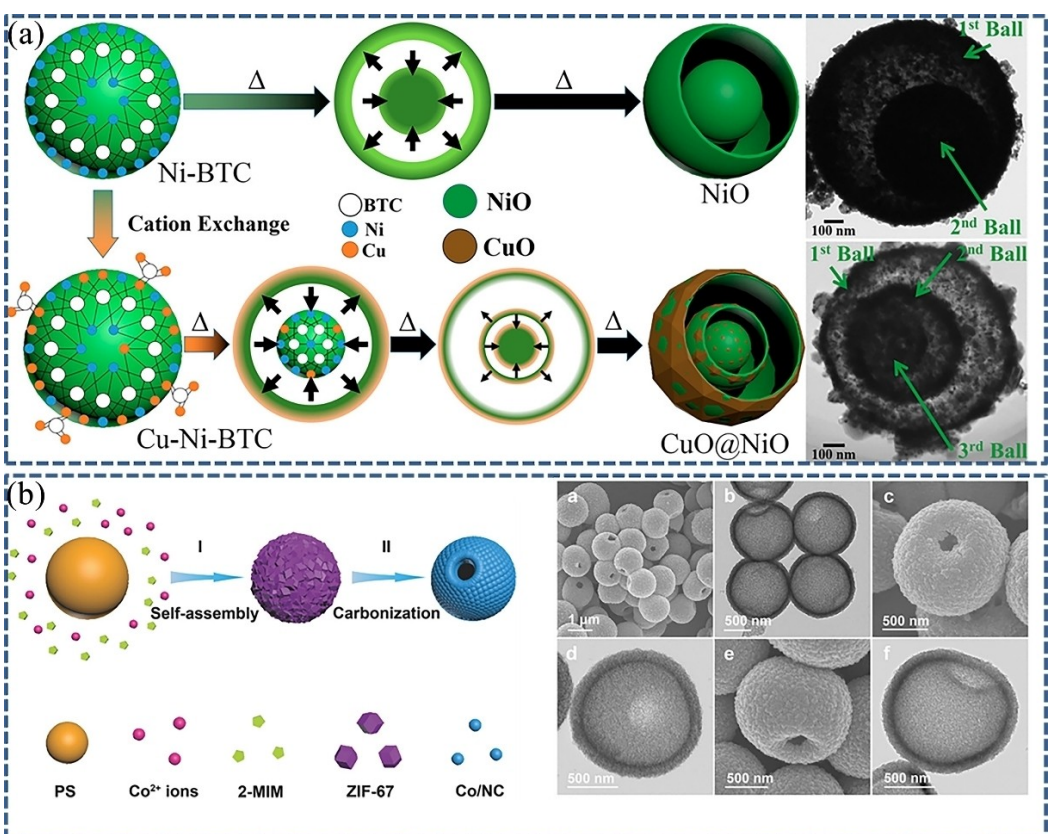


Figure 13. (a) Metal-organic skeleton (MOF) converted to multilayer hollow structure by cation exchange process.^[129] (b) Schematic diagram of single-pore Co/NC hollow particles. FESEM and TEM of single-pore Co/NC hollow particles.^[130]

the surface of Co/NC hollow particles can be attributed to the strong gas outflow resulting from the decomposition of PS spheres. Homogeneous PS microspheres were prepared via surfactant-free emulsion polymerization and further functionalized using polyvinylpyrrolidone. The growth of MOFs shell layer was achieved by introducing $\text{Co}(\text{NO}_3)_2$ metal source and 2-methylimidazole (2-MIM) organic ligand into the reaction system. This resulted in a core-shell structure with a presence of hollow interior as well. Increasing the heating rate from $1^{\circ}\text{Cmin}^{-1}$ to $5^{\circ}\text{Cmin}^{-1}$ and then to $10^{\circ}\text{Cmin}^{-1}$, continuous structural evolution from small-hole hollow particles to larger-hole hollow particles and finally cracked bowl-like shells could be observed for Co/NC materials obtained during pyrolysis process. It should be noted that pore size is influenced by heating rate during pyrolysis; higher heating rates lead to faster degradation of PS microspheres.

The large surface area property of 3D structured carbon materials can expose the active sites to a higher extent. Generally, the construction of three-dimensional structures involves the use of metal foams as substrates (nickel foam, iron foam, copper foam), the growth of arrays of MOFs on their networks, and finally the formation of well-formed three-dimensional hierarchical structured materials derived from MOFs. Yu et al reported a strategy for the synthesis of three-dimensional hierarchical structures.^[131] Electrochemical deposition was employed to achieve the ordered growth of Co-N-C nanosheets

on carbon mats. Subsequently, these nanoclusters were combined with 2-methylimidazole to obtain the desired composites through pyrolysis. Notably, a coexistence of Co^0 and Co^{2+} facilitated bifunctional catalysis in this hierarchical structure. This unique architecture not only enhances electron transport but also significantly increases the number of active sites. The Co and N active sites within the Co/NC composite exhibit the highest adsorption energies for OOH^* intermediates, while C active sites demonstrate superior adsorption energies for O^* intermediates. These findings suggest that the crucial steps in oxygen evolution reaction (OER) and oxygen reduction reaction (ORR) involve the formation and decomposition of OOH^* and O^* intermediates, respectively. Conformal design can be implemented either prior to or after carbonization of metal-organic frameworks (MOFs), ensuring consistency throughout their transformation process. It is worth noting that certain carbon materials may undergo reorganization post-pyrolysis, further emphasizing the significance of three-dimensional hierarchical structures in enhancing performance.

The morphology of composites derived from MOFs is designed by manipulating the synthesis method, adjusting the metal sites, modifying the type or concentration of organic ligands, and incorporating soft or hard templates. Upon pyrolysis, materials with diverse morphologies can be obtained. The ultimate objective behind designing specific morphologies is to enhance catalytic performance.

4.2. Component Design of MOF-Derived Composite Catalysts

Enhancing the intrinsic characteristics of electrocatalysts through tailored design of MOF derivative components constitutes a pivotal stage in experimental design. Specifically, the regulation of electrocatalytic activity is closely linked to the composition of electrocatalyst components. Commonly encountered MOF derivatives encompass transition metal-based, rare earth-based, bi-MOF, and mono-atomic MOF derivatives based on their active constituents. Transition metal-based MOFs are those in which the central metal is a transition metal, and the common ones are Fe, Co, Ni, Zn, Cu, and so on. Transition metal elements have catalytic properties because of the unfilled nature of their own 3d orbitals. Therefore, these MOFs are commonly used as precursors to form derivatives after a series of steps.

Hu et al. reported a nickel-cobalt-containing mixed-metal phosphide nanocartridge synthesized based on a metal-organic skeletons (MOFs) strategy.^[132] This nanobox material exhibits exceptional electrochemical activity and long-term stability. As depicted in Figure 14(a), the authors employed a surfactant-mediated approach to synthesize ZIF-67 cubes, which were subsequently reacted with nickel salts to generate Ni-Co layered double hydroxides on their surfaces, followed by pyrolysis to obtain the desired catalysts. This was achieved by utilizing Co-MOF as a precursor for spinel derivatization. Furthermore, the incorporation of Ni^{2+} not only enhances electrical conductivity but also introduces novel active sites. Nickel-based MOF derivatives also serve as promising candidates for OER catalysts. As shown in Figure 14(b), Yan et al. reported the composite of Ni_2P derived from nickel-based MOF

(MOF-74) with graphene for OER catalysts. Because of the short distance between Ni and carbon atoms in MOF-74, Ni_2P was doped into the graphene surface during the phosphatization process. $\text{Ni}_2\text{P}/\text{rGO}$ has a large surface area and good active site dispersion.^[133] Therefore, it exhibits excellent OER performance ($\eta = 260 \text{ mV}@10 \text{ mA cm}^{-2}$). Phosphides, sulfides, and oxides, which are derived via MOF, make highly excellent electrocatalysts.

Rare-earth-based MOFs primarily utilize rare-earth metals as metal centers. The rare earth elements consist of 17 elements, including La, Ce, Pr, Nd, Pm, Sm, Eu, Gd, Tb, Dy, Ho, Er, Tm, Yb, Lu, Sc, and Y. With the exception of lanthanum (La), most rare earth elements lack 5 d orbital electrons. The presence of empty orbitals facilitates efficient electron transfer pathways and enhances the catalytic properties of rare earth compounds. Notably, CeO_2 , Sm_2O_3 , and La_2O_3 , among other rare earth metal oxides, have been demonstrated to be beneficial to the performance of electrocatalysts. In comparison to transition metal elements, rare earth elements have distinctive 4f orbitals. In terms of electronic structure, the fully filled 5 s₂ and 5 p₆ of rare earth elements are outside the 4f orbitals and show a weak shielding effect on the 4f orbitals. Whereas, the incompletely filled 4f orbitals serve as good and suitable electron acceptors. Moreover, rare earth elements with a higher coordination number offer more possibilities for the formation of new types of MOFs.^[134] In addition, rare earth elements are very oxygen-friendly, and rare earth MOFs form rare earth oxides more easily through the usual pyrolysis method of carbon material forming. Therefor, rare earth oxides are recognized as outstanding doping materials for tuning the electronic structure of transition metals as well as enhancing their catalytic properties.^[135] Most

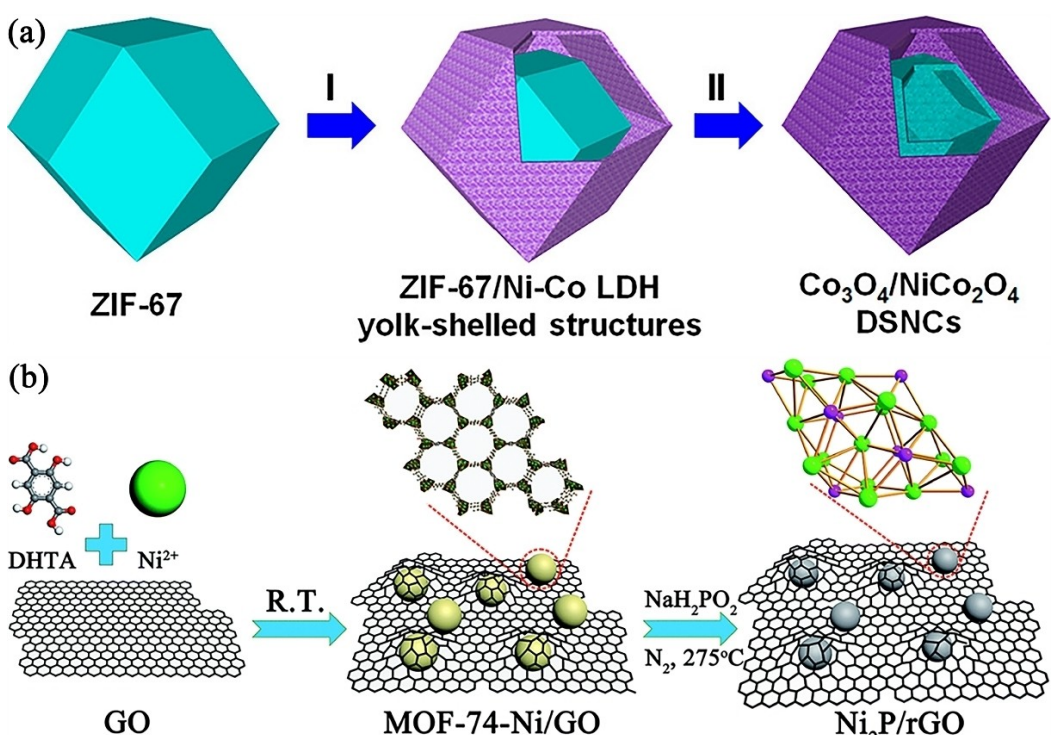


Figure 14. (a) Graphical representation of the forming process of $\text{Co}_3\text{O}_4/\text{NiCo}_2\text{O}_4$ DSNCs.^[132] (b) Synthesis procedure for $\text{Ni}_2\text{P}/\text{rGO}$ illustrated.^[133]

of the work indicated that rare-earth oxides are able to reconfigure the surface chemistry and optimize the catalytic performance through the effect of electron-orbital coupling.^[136–138] Among the scarce reports on rare-earth metal MOFs available currently, the majority focus on cerium (Ce) and lanthanum (La). Kang et al. prepared three-dimensional rosaceous CeO₂ (CeO₂@NC) composites by encapsulating them with nitrogen-doped carbon (NC) composites for the enhancement of oxygen reduction and oxygen precipitation reaction activities (Figure 15(a)).^[139] The Ce-MOF-derived CeO₂ modulated the compound's oxygen vacancy concentration and electronic structure, and the abundant oxygen vacancies were the main reason for the enhanced ORR activity of the material. After assembling into a zinc-air battery, the energy efficiency was 57.3% for 140 hours of cycling, which was better. Li et al. relocated into nitrogen-doped porous carbon after derivatization of L₂O₃/Ni_xP_y nanoparticles via LaNi-MOF (Figure 15(b)).^[140] The electronic structure of the catalyst was adjusted by introducing La₂O₃, while the stability of the catalyst was improved. Although there is less information about rare-earth MOFs applied to zinc-air batteries, metal-organic framework (MOF) materials doped with rare-earth elements are plentiful. Luo et al. demonstrated that Pt/CeO_x/C electrocatalysts based on Ce-based MOF structures are effective electrocatalysts for ORR and H₂/O₂ microlaminar flow fuel cells.^[141] The results indicated that the interplay of Pt nanoparticles and Ce³⁺ species

in Ce-based modified MOF CeO_x resulted in higher ORR activity and durability than commercial Pt/C. Overall, the rare earth-based MOF-derived composites could significantly contribute to the electrocatalytic performance.

MOFs materials could be derived into phosphides, sulfides, oxides etc., and could also be compounded with other components to form derivatives. For example, different kinds of MOFs are compounded. The most common example of dual MOF composite is ZIF-8 and ZIF-67. Wang et al. composited ZIF-8 and ZIF-67 into a core-shell structure transformed into a multilayer porous structure co-doped with cobalt and nitrogen.^[142] The synthesized catalysts possess a distinctive hierarchical micro/mesoporous structure comprising internal micropores and external mesopores. The core-shell architecture consists of ZIF-8@ZIF-67, with ZIF-8 serving as the core to facilitate the uniform pyrolysis of the ZIF-67 shell, thereby resulting in an even distribution of Co-N_x active sites. The incorporation of double MOF composites not only introduces a novel structural design but also enhances the density of active sites. This represents a deliberate design choice for the catalyst's active materials. Currently, researchers are focusing their attention on single-atom catalysts, which involve dispersing metal atoms at an atomic level onto a carrier material. Such materials exhibit superior dispersion characteristics and demonstrate high activity akin to homogeneous catalysts. Yang et al. encapsulated small Co nanoparticles in several layers of graph-

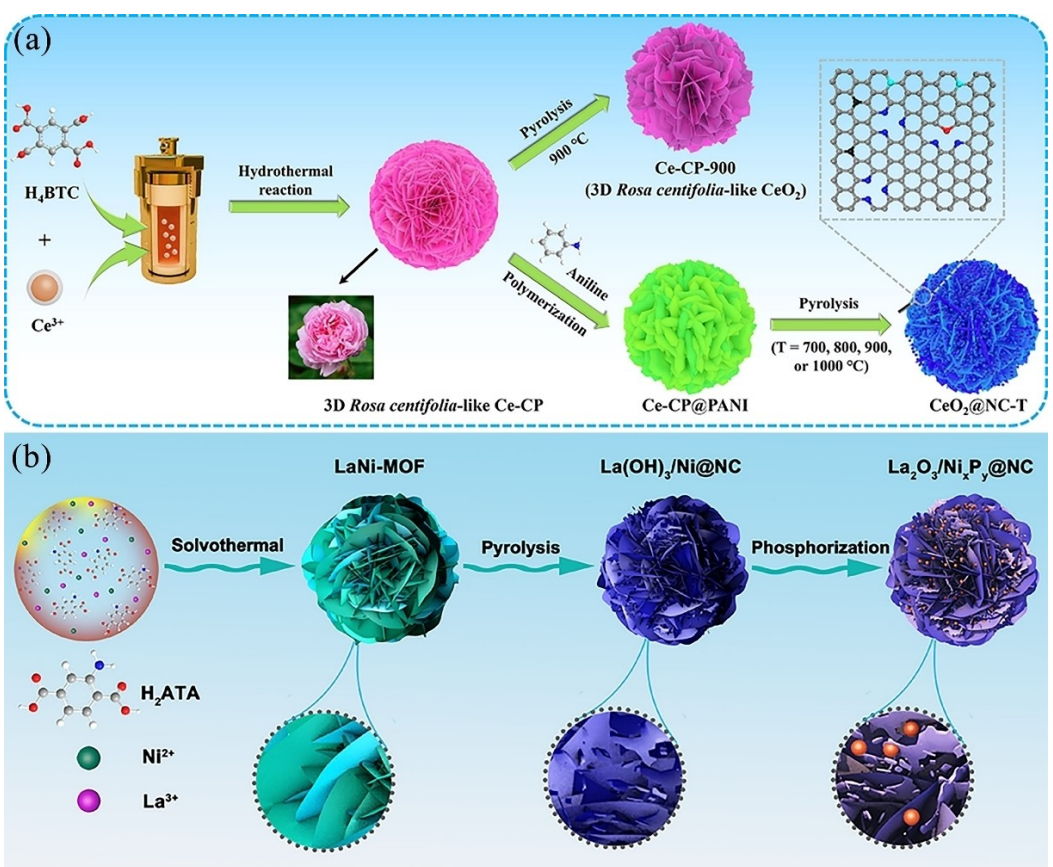


Figure 15. (a) Diagram of the synthesis of CeO₂@NC-T.^[139] (b) Fabrication Process of the La₂O₃/Ni_xP_y@NC.^[140]

ite nanopores modified by Co-SAs using MOF as a substrate. This work maximized the utilization of transition metal actives, as well as optimized the synergistic interaction between Co nanoparticles and Co single atoms, preventing nanoparticle cluster and thus strengthening the catalytic activity of the catalysts, which reached a half-wave potential of 0.871 V. The said catalysts demonstrated excellent performances in both liquid zinc-air batteries and flexible solid-state batteries. Among them, the flexible solid-state battery was able to cycle for 50 hours.^[143] Transformation of MOFs into single-atom catalysts can be achieved through either direct carbonization or acid washing post-carbonization. Chen et al. investigated the coupled evolution of monatomic cobalt-metal sites and Co-N-C sites during the pyrolysis of ZnCo-MOF.^[144] The authors also demonstrated that the utilization of a sulfur-assisted site purification strategy for removing metal particles did not result in a decrease in ORR activity, thereby suggesting the predominant role played by single-atom cobalt sites in the catalytic process. Fe, Co, and Ni single atoms have become increasingly reported as the leading protagonists of single-atom catalysts. Based on the popularization of the synthesis method of this type of catalyst, Mn and Cu single atoms have also become active substances in oxygen electrocatalysts, providing another way of studying new bifunctional catalysts.^[145–147]

The application of bifunctional oxygen electrocatalysts has been reported for metal-organic framework (MOF) materials, with a wide range of MOFs being utilized as precursors to generate MOF derivatives through subsequent steps such as pyrolysis and acid washing. These MOFs exhibit notable characteristics including high specific surface area, flexible chemical composition, and most importantly, a significantly large capacity for modification. This paper lists some of the MOF-derived catalyst material properties as an illustration of the superiority of MOF-based catalysts (Table 2). Compared with other bifunctional catalysts, MOF-based catalysts are in a position to sustain the framework structure of MOF as well as the high porosity, which more easily allows the bifunctional catalysts to have highly dispersed active sites.

5. Conclusions and Perspectives

The rational design of efficient, cost-effective, and stable electrocatalysts is crucial for achieving the large-scale utilization of rechargeable zinc-air batteries. Currently, MOF-derived composites represent the most typical bifunctional electrocatalysts. It is widely acknowledged that the porous structure and tunable chemical components of MOFs are their major advantages as electrocatalysts. Carbon-based materials derived from MOFs, serving as sacrificial templates, exhibit remarkable characteristics such as high activity, conductivity, and stability. This offers novel possibilities for replacing noble metal catalysts. In this study, three types of metal-organic framework bifunctional catalysts (pristine MOFs, MOF derivatives, and composite derivatives) are presented. Each material possesses its own strengths and weaknesses. Pristine MOFs act as pyrolysis-free catalysts with high activity to minimize thermal energy generation during preparation; however, they suffer from weak conductivity hindering rapid electron transfer. Various types of MOF derivatives exist including oxides, sulfides, phosphides, nitrides, alloy materials, and carbon-based materials.

The three materials all have their own advantages and shortcomings. Pristine MOFs exhibit high activity as a pyrolysis-free catalyst, reducing the thermal energy generated during preparation. However, they suffer from extremely weak conductivity, hindering rapid electron transfer. Various types of MOF derivatives (oxides, sulfides, phosphides, nitrides, alloy materials, and carbon-based materials) have been developed to effectively enhance catalytic activity by incorporating heteroatoms such as O, S, P, and N with transition metals to alter the electronic structure. Catalytic activity can be modulated through heteroatom doping or strong metal coupling (alloys), leading to changes in crystalline phase or valence state. Nevertheless, some MOF-derived compounds are reported to be highly unstable under high potential conditions for oxygen evolution reaction (OER), easily oxidizing into oxides or hydroxides. Therefore, more comprehensive analytical techniques are required for investigating active components. MOF-derived carbon-based materials utilize the original framework of MOFs as a carbon skeleton and facilitate mass-charge transport

Table 2. Electrochemical performance of MOF-based bifunctional catalysts for Zn-air batteries.

Electrode material (Based material)	Initial MOF	ORR ($E_{1/2}$)/V	OER ($\eta = 10 \text{ mA cm}^{-2}$)/mV	$\Delta E(E_{10}-E_{1/2})/V$	Ref
Co–Fe alloy NPs	ZIF-67	0.87	273	0.633	[148]
Ni ₂ P/NiCoP	ZIF-8	0.898	330	0.662	[69]
Co/CoO	ZIF-67	0.843	356	0.743	[149]
FeCo-WC heterostructure	ZIF-8/ZIF-67	0.889	290	0.631	[150]
Co ₃ Fe ₇ Fe/Co–N dual single-atom sites	MIL-53	0.880	342	0.692	[151]
Fe–N–C	Porphyrin Based MOFs/ZIF-8	0.920	290	0.600	[152]
Co/FeCo@Fe(Co) ₃ O ₄ heterostructure	ZIF-67/MIL-101	0.840	373	0.763	[153]
FeCu-BTC@WO ₃ -WC	FeCu-BTC	0.810	249	0.669	[154]
FeNi alloy nanoparticles	Ni-based MOF	0.840	330	0.720	[155]
Fe ₃ C/CoFe ₂ O ₄	MIL-53	0.840	340	0.730	[156]

while exhibiting satisfactory electrical conductivity. However, metal nanoparticles derived from MOFs exhibit the drawback of high aggregation, which significantly impedes chemical reactions due to increased surface energy. Consequently, some studies have proposed incorporating active substances in MOFs with carbon materials (such as carbon nanotubes and graphene) or catalytically generating carbon nanotubes through transition metals within MOFs. This approach effectively prevents the aggregation of metal nanoparticles and enhances the activity of ORR and OER. Additionally, composite-derived materials based on MOFs are designed to prevent agglomeration of metal nanoparticles by employing template methods or compositing with other MOFs. Researchers have also developed specialized hierarchical structures for MOFs to increase material surface area and achieve more uniform dispersion of active substances on carbon carriers. Furthermore, the strong interactions between metal nanoparticles and pre-modified carbon carriers further enhance electrocatalytic activity.

The above provides a brief summary of the advantages and disadvantages associated with bifunctional catalysts employing metal-organic frameworks (MOFs). However, there are significant challenges in the practical application of this material in rechargeable zinc-air batteries. Firstly, MOF synthesis allows for diverse morphologies and unique structures. Nevertheless, the process of synthesizing MOF precursors remains complex, limiting its scalability. Additionally, MOF derivatives are typically obtained through calcination which leads to high precursor consumption and low output rates. Therefore, it is necessary to develop simplified synthesis strategies with enhanced productivity. Secondly, current research focuses on developing single-atom catalysts to maximize the utilization of active substances within MOFs. This requires advanced testing techniques such as synchrotron radiation, spherical aberration electron microscopy, and scanning tunneling microscopy to characterize the single atoms indicated by these catalysts. However, these testing techniques are not yet commonly employed in commercial applications. Thirdly, doping MOFs with heteroatoms usually involves pyrolysis or vapor-phase deposition methods to maintain precursor morphology. During pyrolysis, uncontrollable decomposition of MOFs occurs making it challenging to precisely control their morphology while doping with heteroatoms; thus, hindering the preparation of catalyst materials with specific structures. Despite the superior performance and lower cost of MOF composite catalysts and their derivatives compared to noble metal catalysts, this data is solely derived from laboratory experiments and has yet to make a significant impact in practical applications. The complexity of its synthesis process limits actual adoption. The widespread implementation of rechargeable zinc-air batteries continues to be hindered by various factors such as variable environments and different catalyst loadings. Consequently, the design and preparation of catalysts should consider the materials' ability to adapt to extreme conditions including high temperature, low temperature, high humidity, and low humidity. Simultaneously, continuous improvements in Zn-air battery devices are necessary while standardizing testing conditions for these batteries.

In conclusion, MOF-based bifunctional oxygen electrocatalysts exhibit great promise as a group of electrocatalyst materials. There is still much ground to cover in the study of MOF-based electrocatalyst preparation. However, the advancement of MOF-based electrocatalysts will also significantly propel the widespread application of rechargeable Zn-air batteries.

Acknowledgements

The authors thank the Guangdong University of Technology Hundred Talents Program (No. 263118136), key Laboratory of Advanced Electrode Materials for Novel Solar Cells for Petroleum and Chemical Industry of China, School of Chemistry and Life Sciences, Suzhou University of Science and Technology (P. R. China) (No. 2024 A109).

Conflict of Interests

The authors declare that they have no known competing financial interests or personal relationships that could have appeared to influence the work reported in this paper.

Data Availability Statement

Data will be made available on request.

Keywords: Metal-organic framework (MOF) • MOF-derived carbon materials • MOF derivatives • Bifunctional electrocatalyst • Zn-air batteries

- [1] J. Lin, X. Zhang, E. Fan, R. Chen, F. Wu, L. Li, *Energy Environ. Sci.* **2023**, *16*, 745–791.
- [2] P. Ruan, S. Liang, B. Lu, H. J. Fan, J. Zhou, *Angew. Chem. Int. Ed.* **2022**, *134*, e202200598.
- [3] Y. F. Guo, S. Zhao, N. Zhang, Z.-L. Liu, P. F. Wang, J. H. Zhang, Y. Xie, T. F. Yi, *Energy Environ. Sci.* **2024**, *17*, 1725–1755.
- [4] X. Xu, H. Liao, L. Huang, S. Chen, R. Wang, S. Wu, Y. Wu, Z. Sun, H. Huang, *Appl. Catal. B* **2024**, *341*, 123312.
- [5] T. Zhou, X. Wu, S. Liu, A. Wang, Y. Liu, W. Zhou, K. Sun, S. Li, J. Zhou, B. Li, J. Jiang, *ChemSusChem* **2024**, *17*, e202301779.
- [6] Y. Kumar, M. Mooste, K. Tammeveski, *Curr. Opin. Electrochem.* **2023**, *38*, 101229.
- [7] Y. Yu, D. Wang, J. Luo, Y. Xiang, *Colloids Surf. A* **2023**, *659*, 130802.
- [8] X. Bi, Y. Jiang, R. Chen, Y. Du, Y. Zheng, R. Yang, R. Wang, J. Wang, X. Wang, Z. Chen, *Adv. Energy Mater.* **2023**, *14*, 2302388.
- [9] J. Park, M. Park, G. Nam, J. S. Lee, J. Cho, *Adv. Mater.* **2015**, *27*, 1396–1401.
- [10] K. W. Leong, Y. Wang, M. Ni, W. Pan, S. Luo, D. Y. C. Leung, *Renewable Sustainable Energy Rev.* **2022**, *154*, 111771.
- [11] Y. Zhang, Y.-P. Deng, J. Wang, Y. Jiang, G. Cui, L. Shui, A. Yu, X. Wang, Z. Chen, *Energy Storage Mater.* **2021**, *35*, 538–549.
- [12] Z. Y. Mei, S. Cai, G. Zhao, Q. Jing, X. Sheng, J. Jiang, H. Guo, *Energy Storage Mater.* **2022**, *50*, 12–20.
- [13] S. Sarkar, A. Biswas, E. E. Siddharthan, R. Thapa, R. S. Dey, *ACS Nano* **2022**, *16*, 7890–7903.
- [14] Y. Li, M. Cui, Z. Yin, S. Chen, T. Ma, *Chem. Sci.* **2020**, *11*, 11646–11671.
- [15] Y. Guo, Y. N. Chen, H. Cui, Z. Zhou, *Chin. J. Catal.* **2019**, *40*, 1298–1310.
- [16] Y. Zhu, Q. Lin, Y. Zhong, H. A. Tahini, Z. Shao, H. Wang, *Energy Environ. Sci.* **2020**, *13*, 3361–3392.

- [17] D. Zhao, Z. Zhuang, X. Cao, C. Zhang, Q. Peng, C. Chen, Y. Li, *Chem. Soc. Rev.* **2020**, *49*, 2215–2264.
- [18] X. Peng, L. Zhang, Z. Chen, L. Zhong, D. Zhao, X. Chi, X. Zhao, L. Li, X. Lu, K. Leng, C. Liu, W. Liu, W. Tang, K. P. Loh, *Adv. Mater.* **2019**, *31*, 1900341.
- [19] D. B. Kumar, W. Nie, Z. Jiang, J. Lee, T. Maiyalagan, *J. Alloys Compd.* **2023**, *960*, 170828.
- [20] S. Chen, H. Liao, X. Xu, R. Wang, Z. Sun, L. Huang, *Inorg. Chem. Front.* **2023**, *10*, 6320–6328.
- [21] Y. Arafat, Y. Zhong, M. R. Azhar, M. Asif, M. O. Tadé, Z. Shao, *EcoMat* **2023**, *5*, e12394.
- [22] T. Li, Y. Liu, Y. Huang, L. Zhang, Z. Chen, W. Yang, G. Shi, J. Zhou, R. Zou, J. Gan, L. Zhong, X. Peng, *Small* **2024**, *20*, 2311675.
- [23] Y. He, J. Yang, Y. Wang, Y. Jia, H. Li, Y. Liu, L. Liu, Q. Tan, *ACS Appl. Mater. Interfaces* **2024**, *16*, 12398–12406.
- [24] Y. Huang, Y. Chen, M. Xu, A. Ly, A. Gili, E. Murphy, T. Asset, Y. Liu, V. De Andrade, C. U. Segre, A. L. Deriy, F. De Carlo, M. Kunz, A. Gurlo, X. Pan, P. Atanassov, I. V. Zenyuk, *Mater. Today* **2023**, *69*, 66–78.
- [25] H. Chang, L.-N. Shi, Y.-H. Chen, P.-F. Wang, T.-F. Yi, *Coord. Chem. Rev.* **2022**, *473*, 214839.
- [26] Z. Li, J. Yang, X. Ge, Y.-P. Deng, G. Jiang, H. Li, G. Sun, W. Liu, Y. Zheng, H. Dou, H. Jiao, J. Zhu, N. Li, Y. Hu, M. Feng, Z. Chen, *Nano Energy* **2021**, *89*, 106314.
- [27] X. Xu, S. Zhang, Q. Zhang, S. Chen, Y. Wu, Z. Sun, *ACS Sustainable Chem. Eng.* **2023**, *11*, 15338–15349.
- [28] S. S. A. Shah, H. K. Zafar, M. S. Javed, M. A. U. Din, S. S. Alarfaji, G. Balkourani, M. Sohail, P. Tsikakras, T. Najam, *Coord. Chem. Rev.* **2024**, *501*, 215565.
- [29] X. Zou, M. Tang, Q. Lu, Y. Wang, Z. Shao, L. An, *Energy Environ. Sci.* **2024**, *17*, 386–424.
- [30] Y. Li, Y. Deng, D. Liu, Q. Ji, X. Cai, *Mater. Chem. Front.* **2024**, *8*, 880–902.
- [31] S. Gao, X. Wang, X. Liu, C. Guo, Q. Liu, G. Hu, *Mater. Chem. Front.* **2024**, *8*, 485–506.
- [32] J. Pan, Y. Y. Xu, H. Yang, Z. Dong, H. Liu, B. Y. Xia, *Adv. Sci.* **2018**, *5*, 1700691.
- [33] K. Harting, U. Kunz, T. Turek, *Zeitschrift für Phys. Chemie* **2012**, *226*, 151–166.
- [34] J. Balamurugan, P. M. Austeria, J. B. Kim, E. S. Jeong, H. H. Huang, D. H. Kim, N. Koratkar, S. O. Kim, *Adv. Mater.* **2023**, *35*, 2302625.
- [35] M. Wang, Z. Chen, Y. Song, Z. Hu, H. Song, S. Dong, D. Yuan, *Inorg. Chem.* **2024**, *63*, 4373–4384.
- [36] Y. P. Deng, Y. Jiang, R. Liang, S. J. Zhang, D. Luo, Y. Hu, X. Wang, J. T. Li, A. Yu, Z. Chen, *Nat. Commun.* **2020**, *11*, 1952.
- [37] X. Zhao, F. Wu, H. Hu, J. Li, Y. Sun, J. Wang, G. Zou, X. Chen, Y. Wang, C. Fernandez, Q. Peng, *Small* **2024**, *20*, 2311268.
- [38] T. Zhou, N. Zhang, C. Wu, Y. Xie, *Energy Environ. Sci.* **2020**, *13*, 1132–1153.
- [39] J. Zou, T. Liang, M. Peng, P. Liu, Z. Li, J. Wen, Z. Li, Y. Yan, X. Yu, X. Zeng, J. Huang, *J. Storage Mater.* **2024**, *84*, 110815.
- [40] X. Han, X. Yu, H. S. Park, *Mater. Chem. Front.* **2024**, *8*, 1536–1562.
- [41] J. Chen, J. Luo, Y. Xiang, Y. Yu, *J. Energy Chem.* **2024**, *91*, 178–193.
- [42] P. Chen, K. Zhang, D. Tang, W. Liu, F. Meng, Q. Huang, J. Liu, *Front. Chem.* **2020**, *8*, 372.
- [43] H. F. Wang, Q. Xu, *Matter* **2019**, *1*, 565–595.
- [44] Z. Wang, Y. Lu, Y. Yan, T. Y. P. Larissa, X. Zhang, D. Wu, H. Zhang, Y. Yang, X. Wang, *Nano Energy* **2016**, *30*, 368–378.
- [45] P. Sapkota, H. Kim, *J. Ind. Eng. Chem.* **2009**, *15*, 445–450.
- [46] S. Ren, X. Duan, S. Liang, M. Zhang, H. Zheng, *J. Mater. Chem. A* **2020**, *8*, 6144–6182.
- [47] S. A. Samad, Z. Fang, P. Shi, J. Zhu, C. Lu, Y. Su, X. Zhuang, *2D Mater.* **2023**, *10*, 022001.
- [48] X. Wang, X. Xu, J. Chen, Q. Wang, *ACS Sustainable Chem. Eng.* **2019**, *7*, 12331–12339.
- [49] H. F. Wang, C. Tang, B. Wang, B. Q. Li, Q. Zhang, *Adv. Mater.* **2017**, *29*, 1702327.
- [50] J. Song, C. Wei, Z.-F. Huang, C. Liu, L. Zeng, X. Wang, Z. J. Xu, *Chem. Soc. Rev.* **2020**, *49*, 2196–2214.
- [51] I. C. Man, H. Y. Su, F. Calle-Vallejo, H. A. Hansen, J. I. Martínez, N. G. Inoglu, J. Kitchin, T. F. Jaramillo, J. K. Nørskov, J. Rossmeisl, *ChemCatChem* **2011**, *3*, 1159–1165.
- [52] G. Fu, Y. Tang, J.-M. Lee, *ChemElectroChem* **2018**, *5*, 1424–1434.
- [53] S. Ren, X. Duan, S. Liang, M. Zhang, H. Zheng, *J. Mater. Chem. A* **2020**, *8*, 6144–6182.
- [54] H. F. Wang, C. Tang, Q. Zhang, *Adv. Funct. Mater.* **2018**, *28*, 1803329.
- [55] X. Liu, G. Zhang, L. Wang, H. Fu, *Small* **2021**, *17*, 2006766.
- [56] X. X. Wang, X. Yang, H. Liu, T. Han, J. Hu, H. Li, G. Wu, *Small Structures* **2021**, *3*, 2100103.
- [57] X. Chen, Z. Zhou, H. E. Karahan, Q. Shao, L. Wei, Y. Chen, *Small* **2018**, *14*, e1801929.
- [58] A. Bieniek, A. P. Terzyk, M. Wiśniewski, K. Roszek, P. Kowalczyk, L. Sarkisov, S. Keskin, K. Kaneko, *Prog. Mater. Sci.* **2021**, *117*, 100743.
- [59] B. Szczęśniak, J. Choma, M. Jaroniec, *J. Colloid Interface Sci.* **2018**, *514*, 801–813.
- [60] A. Indra, T. Song, U. Paik, *Adv. Mater.* **2018**, *30*, 1705146.
- [61] S. Ren, P. Zhang, X. Tang, H. Zheng, Z. Wan, *J. Storage Mater.* **2024**, *83*, 110660.
- [62] L. Zhang, L.-L. Liu, J.-J. Feng, A.-J. Wang, *J. Colloid Interface Sci.* **2024**, *661*, 102–112.
- [63] W. Cheng, X. Zhao, H. Su, F. Tang, W. Che, H. Zhang, Q. Liu, *Nat. Energy* **2019**, *4*, 115–122.
- [64] M. F. Sanad, A. R. Puente Santiago, S. A. Tolba, M. A. Ahsan, O. Fernandez-Delgado, M. Shawky Adly, E. M. Hashem, M. Mahrous Abdouh, M. S. El-Shall, S. T. Sreenivasan, N. K. Allam, L. Echegoyen, *J. Am. Chem. Soc.* **2021**, *143*, 4064–4073.
- [65] X. Zheng, Y. Cao, D. Liu, M. Cai, J. Ding, X. Liu, J. Wang, W. Hu, C. Zhong, *ACS Appl. Mater. Interfaces* **2019**, *11*, 15662–15669.
- [66] H. Mei, Y. Mei, S. Zhang, Z. Xiao, B. Xu, H. Zhang, L. Fan, Z. Huang, W. Kang, D. Sun, *Inorg. Chem.* **2018**, *57*, 10953–10960.
- [67] G. Hai, X. Jia, K. Zhang, X. Liu, Z. Wu, G. Wang, *Nano Energy* **2018**, *44*, 345–352.
- [68] H. Pourfarzad, M. Shabani-Nooshabadi, M. R. Ganjali, *J. Power Sources* **2020**, *451*, 227768.
- [69] H. Lei, W. Li, J. Fei, S. Guo, Y. Liu, Q. Liu, L. Cheng, Y. Huang, *J. Environ. Chem. Eng.* **2023**, *11*, 111549.
- [70] F. Zhang, L. Chen, Y. Zhang, Y. Peng, X. Luo, Y. Xu, Y. Shi, *Chem. Eng. J.* **2022**, *447*, 137490.
- [71] C. Fang, X. Tang, Q. Yi, *Appl. Catal. B* **2024**, *341*, 123346.
- [72] Q. Wang, L. Wang, S. Zhang, Z. Chen, W. Peng, Y. Li, X. Fan, *J. Colloid Interface Sci.* **2025**, *677*, 800–811.
- [73] K. Chen, C. Chen, J. Long, G. Zhou, *Appl. Surf. Sci.* **2024**, *657*, 159803.
- [74] M. Gopalakrishnan, W. Kao-lan, M. Rittiruam, S. Praserthdam, P. Praserthdam, W. Limphirat, M. T. Nguyen, T. Yonezawa, S. Kheawhom, *ACS Appl. Mater. Interfaces* **2024**, *16*, 11537–11551.
- [75] C. Lv, B. Li, Y. Ren, G. Zhang, Z. Lu, L. Li, X. Zhang, X. Yang, X. Yu, *Chem. Eng. J.* **2024**, *495*, 153670.
- [76] H.-S. Fan, F.-X. Ma, Z.-H. Liu, W.-H. Wang, Z.-Q. Liu, X.-Y. Liang, Y. Du, Y.-Y. Li, L. Zhen, C.-Y. Xu, *Rare Met.* **2024**. <https://doi.org/10.1007/s12598-024-02676-y>.
- [77] K. Wu, D. Wang, Q. Fu, T. Xu, Q. Xiong, S. G. Peera, C. Liu, *Inorg. Chem.* **2024**, *63*, 11135–11145.
- [78] H. Xu, L. Xiao, P. Yang, X. Lu, L. Liu, D. Wang, J. Zhang, M. An, *J. Colloid Interface Sci.* **2023**, *638*, 242–251.
- [79] J. Liu, J. Yu, X. Wang, M. Cheng, S. Sun, S. Hu, C. Li, Z. Wang, *ACS Appl. Mater. Interfaces* **2023**, *15*, 59482–59493.
- [80] H. Yu, D. Liu, K. Srinivas, F. Ma, Z. Zhang, M. Wang, Y. Wu, Y. Wang, X. Li, Y. Chen, *J. Alloys Compd.* **2023**, *949*, 169863.
- [81] U. Bhardwaj, P. Janjani, R. Sharma, H. S. Kushwaha, *J. Electron. Mater.* **2022**, *52*, 917–924.
- [82] W. Guo, Z. Zhang, P. Chen, X. Luan, J. Dou, J. Bai, H. Fang, W. Shi, B. Zhou, *Microporous Mesoporous Mater.* **2022**, *331*, 111639.
- [83] I. Das, M. T. Noori, M. Shaikh, M. M. Ghangrekar, R. Ananthakrishnan, *ACS Appl. Energ. Mater.* **2020**, *3*, 3512–3520.
- [84] J. W. Huang, Y. B. Chen, J. M. Yang, H. B. Zhu, H. Yang, *Electrochim. Acta* **2021**, *366*, 137408.
- [85] L. Chen, Z. Song, Z. Li, Z. Yang, J. Zhang, H. Li, Z. Zheng, *J. Alloys Compd.* **2022**, *894*, 162456.
- [86] K. Min, S. Kim, E. Lee, G. Yoo, H. C. Ham, S. E. Shim, D. Lim, S.-H. Baeck, *J. Mater. Chem. A* **2021**, *9*, 17344–17352.
- [87] Z. Luo, F. Wei, J. Gong, L. Wang, Z. Huang, T. T. Isimjan, X. Yang, *Inorg. Chem. Front.* **2023**, *10*, 7333–7342.
- [88] J. Hwang, A. Ejsmont, R. Freund, J. Goscianska, B. V. K. J. Schmidt, S. Wuttke, *Chem. Soc. Rev.* **2020**, *49*, 3348–3422.
- [89] B. Zhu, D. Xia, R. Zou, *Coord. Chem. Rev.* **2018**, *376*, 430–448.
- [90] C. Cheng, C. Zhi, Z.-T. Sun, Y.-Q. Ming, T.-T. Xiang, Q.-C. Zhu, Z.-R. Wu, B. Li, Y. Li, C. Jin, Y. Cao, J. Yang, *Rare Met.* **2024**, *43*, 1524–1536.
- [91] H. Liu, Y. Liu, S. Mehdi, X. Wu, T. Liu, B. Zhou, P. Zhang, J. Jiang, B. Li, *Adv. Sci.* **2021**, *8*, 2101314.
- [92] Y. Xiong, Z. Jiang, L. Gong, X. Tian, C. Song, T. Maiyalagan, Z.-J. Jiang, J. Colloid Interface Sci. **2023**, *649*, 36–48.

- [93] L. Zhao, J. Zhang, G. Jin, Z.-J. Jiang, Z. Jiang, *J. Colloid Interface Sci.* **2024**, *668*, 525–539.
- [94] L. Ye, W. Chen, Z. Jiang, Z. Jiang, *Carbon Energy* **2024**, *6*, e457.
- [95] Y. Rao, S. Chen, Q. Yue, Y. Kang, *ACS Catal.* **2021**, *11*, 8097–8103.
- [96] X. He, F. Yin, G. Li, *Int. J. Hydrogen Energy* **2015**, *40*, 9713–9722.
- [97] L. Yan, Z. Xu, W. Hu, J. Ning, Y. Zhong, Y. Hu, *Nano Energy* **2021**, *82*, 105710.
- [98] R. Jena, S. Bhattacharyya, N. Bothra, V. Kashyap, S. K. Pati, T. K. Maji, *ACS Appl. Mater. Interfaces* **2023**, *15*, 27893–27904.
- [99] Y. Niu, Y. Yuan, Q. Zhang, F. Chang, L. Yang, Z. Chen, Z. Bai, *Nano Energy* **2021**, *82*, 105699.
- [100] R. Wang, Y. Yang, X. Xu, S. Chen, A. Trukhanov, R. Wang, L. Shao, X. Lu, H. Pan, Z. Sun, *Inorg. Chem. Front.* **2023**, *10*, 1348–1356.
- [101] X. Xu, R. Wang, S. Chen, A. Trukhanov, Y. Wu, L. Shao, L. Huang, Z. Sun, *Inorg. Chem. Front.* **2022**, *9*, 5507–5516.
- [102] F. Pei, M. Chen, F. Kong, Y. Huang, X. Cui, *Appl. Surf. Sci.* **2022**, *587*, 152922.
- [103] X. Liu, Z. Yin, M. Cui, L. Gao, A. Liu, W. N. Su, S. Chen, T. Ma, Y. Li, *J. Colloid Interface Sci.* **2022**, *610*, 653–662.
- [104] X. Shi, J. Du, L. Jia, Y. Gong, J. Jin, H. Wang, R. Wang, L. Zhao, B. He, *ACS Appl. Mater. Interfaces* **2023**, *15*, 26766–26777.
- [105] L. Wu, J. Li, C. Shi, Y. Li, H. Mi, L. Deng, Q. Zhang, C. He, X. Ren, *J. Mater. Chem. A* **2022**, *10*, 16627–16638.
- [106] C. Yao, J. Li, Z. Zhang, C. Gou, Z. Zhang, G. Pan, J. Zhang, *Small* **2022**, *18*, 210894.
- [107] S. H. Gillani, M. Sohail, L. Abu El Maati, R. Altuijri, R. Zairov, M. F. Nazar, I. Ahmad, *J. Alloys Compd.* **2024**, *976*, 172931.
- [108] S. H. Hsu, S. F. Hung, H. Y. Wang, F. X. Xiao, L. Zhang, H. Yang, H. M. Chen, J. M. Lee, B. Liu, *Small Methods* **2018**, *2*, 1800001.
- [109] J. Li, Y. Kang, W. Wei, X. Li, Z. Lei, P. Liu, *Chem. Eng. J.* **2021**, *407*, 127961.
- [110] Q. Yan, X. Duan, Y. Liu, F. Ge, H. Zheng, *J. Mater. Chem. A* **2023**, *11*, 1430–1438.
- [111] A. Kundu, A. Samanta, C. R. Raj, *ACS Appl. Mater. Interfaces* **2021**, *13*, 30486–30496.
- [112] H. Huang, Q. Liang, H. Guo, Z. Wang, G. Yan, F. Wu, J. Wang, *Small* **2024**, *20*, 202310318.
- [113] M. Sun, D. Davenport, H. Liu, J. Qu, M. Elimelech, J. Li, *J. Mater. Chem. A* **2018**, *6*, 2527–2539.
- [114] C. Guo, Y. Li, W. Liao, Y. Liu, Z. Li, L. Sun, C. Chen, J. Zhang, Y. Si, L. Li, *J. Mater. Chem. A* **2018**, *6*, 13050–13061.
- [115] J. Han, X. Meng, L. Lu, J. Bian, Z. Li, C. Sun, *Adv. Funct. Mater.* **2019**, *29*, 1808872.
- [116] J. Wu, L. Hu, N. Wang, Y. Li, D. Zhao, L. Li, X. Peng, Z. Cui, L.-J. Ma, Y. Tian, X. Wang, *Appl. Catal. B* **2019**, *254*, 55–65.
- [117] X. Sun, S. Sun, S. Gu, Z. Liang, J. Zhang, Y. Yang, Z. Deng, P. Wei, J. Peng, Y. Xu, C. Fang, Q. Li, J. Han, Z. Jiang, Y. Huang, *Nano Energy* **2019**, *61*, 245–250.
- [118] X. Han, X. Ling, Y. Wang, T. Ma, C. Zhong, W. Hu, Y. Deng, *Angew. Chem. Int. Ed.* **2019**, *58*, 5359–5364.
- [119] K. Im, J. H. Jang, J. Heo, D. Kim, K. S. Lee, H. K. Lim, J. Kim, S. J. Yoo, *Appl. Catal. B* **2022**, *308*, 121220.
- [120] H. Tian, A. Song, P. Zhang, K. Sun, J. Wang, B. Sun, Q. Fan, G. Shao, C. Chen, H. Liu, Y. Li, G. Wang, *Adv. Mater.* **2023**, *35*, 2210714.
- [121] Q. Wang, Y. Yang, F. Sun, G. Chen, J. Wang, L. Peng, W. T. Chen, L. Shang, J. Zhao, D. Sun-Waterhouse, T. Zhang, G. I. N. Waterhouse, *Adv. Energy Mater.* **2021**, *11*, 2100219.
- [122] H. Chang, Y.-F. Guo, X. Liu, P. F. Wang, Y. Xie, T. F. Yi, *Appl. Catal. B* **2023**, *327*, 122469.
- [123] L. Zhang, Y. Zhu, Z. Nie, Z. Li, Y. Ye, L. Li, J. Hong, Z. Bi, Y. Zhou, G. Hu, *ACS Nano* **2021**, *15*, 13399–13414.
- [124] J. W. Nai, Y. Lu, L. Yu, X. Wang, X. W. Lou, *Adv. Mater.* **2017**, *29*, 1703870.
- [125] X. F. Lu, Y. Chen, S. B. Wang, S. Y. Gao, L. Xiong Wen David, *Adv. Mater.* **2019**, *31*, 1902339.
- [126] W. Cheng, X. F. Lu, D. Luan, X. W. Lou, *Angew. Chem. Int. Ed.* **2020**, *59*, 18234–18239.
- [127] Z. X. Cai, Z. L. Wang, J. Kim, Y. Yamauchi, *Adv. Mater.* **2019**, *31*, e1804903.
- [128] H. Kim, M. S. Lah, *Dalton Trans.* **2017**, *46*, 6146–6158.
- [129] W. Guo, W. Sun, Y. Wang, *ACS Nano* **2015**, *9*, 11462–11471.
- [130] C. Fan, W. Dong, Y. Saira, Y. Tang, G. Fu, J. M. Lee, *Small* **2023**, *19*, 2302738.
- [131] C. Fan, X. Wu, M. Li, X. Wang, Y. Zhu, G. Fu, T. Ma, Y. Tang, *Chem. Eng. J.* **2022**, *431*, 133829.
- [132] X. Wang, J. Wang, P. Wang, L. Li, X. Zhang, D. Sun, Y. Li, Y. Tang, Y. Wang, G. Fu, *Adv. Mater.* **2022**, *34*, 2206540.
- [133] M. Li, X. Wang, K. Liu, H. Sun, D. Sun, K. Huang, Y. Tang, W. Xing, H. Li, G. Fu, *Adv. Mater.* **2023**, *35*, 2302462.
- [134] X. Wang, M. Li, P. Wang, D. Sun, L. Ding, H. Li, Y. Tang, G. Fu, *Small Methods* **2023**, *7*, 2300100.
- [135] B. Y. Guan, Y. Le, X. W. Lou, *Adv. Sci.* **2017**, *4*, 1700247.
- [136] P. Yu, L. Wang, F. Sun, Y. Xie, X. Liu, J. Ma, X. Wang, C. Tian, J. Li, H. Fu, *Adv. Mater.* **2019**, *31*, e1901666.
- [137] H. Hu, B. Guan, B. Xia, X. W. Lou, *J. Am. Chem. Soc.* **2015**, *137*, 5590–5595.
- [138] L. Yan, H. Jiang, Y. Xing, Y. Wang, D. Liu, X. Gu, P. Dai, L. Li, X. Zhao, *J. Mater. Chem. A* **2018**, *6*, 1682–1691.
- [139] Y. Yang, Y. Xiao, L. Zhang, H.-T. Wang, K.-H. Chen, W.-X. Lin, N. Jin, C. Sun, Y.-C. Shao, J.-L. Chen, J. Qian, L. Han, *Appl. Catal. B* **2024**, *347*, 123792.
- [140] Y. Kang, W. Wang, J. Li, Y. Mi, H. Gong, Z. Lei, *J. Colloid Interface Sci.* **2020**, *578*, 796–804.
- [141] X. Zhang, F. Yang, S. Sun, K. Wei, H. Liu, G. Li, Y. Sun, X. Li, J. Qian, S. Du, M. Li, Y. Lu, C. Xia, S. Che, Y. Li, *J. Colloid Interface Sci.* **2024**, *657*, 240–249.
- [142] W.-J. Niu, W.-W. Zhao, Y.-Y. Yan, C.-Y. Cai, B.-X. Yu, R.-J. Li, *J. Colloid Interface Sci.* **2024**, *675*, 989–998.
- [143] L. Li, N. Li, J.-W. Xia, S.-L. Zhou, X.-Y. Qian, F.-X. Yin, G.-H. Dai, G.-Y. He, H.-Q. Chen, *Nano Res.* **2023**, *16*, 9416–9425.
- [144] L. Li, H. Peng, Y. Kang, Y. Hao, F. Liu, H. Xin, H. Kang, W. Wang, Z. Lei, *ACS Appl. Nano Mater.* **2023**, *6*, 4349–4359.
- [145] Z. Zhang, S. Liu, X. Li, T. Qin, L. Wang, X. Bo, Y. Liu, L. Xu, S. Wang, X. Sun, Y. Lu, F. Luo, S. Liu, *ACS Appl. Mater. Interfaces* **2018**, *10*, 22023–22030.
- [146] Z. Hu, Z. Zhang, Z. Li, M. Dou, F. Wang, *ACS Appl. Mater. Interfaces* **2017**, *9*, 16109–16116.
- [147] W. Zhao, G. Wan, C. Peng, H. Sheng, J. Wen, H. Chen, *ChemSusChem* **2018**, *11*, 3473–3479.
- [148] X. He, L. Chang, H. Wu, G. Liu, Y. Zhang, A. Zhou, *J. Alloys Compd.* **2023**, *967*, 171709.
- [149] Y. Luo, M. Wen, J. Zhou, Q. Wu, G. Wei, Y. Fu, *Small* **2023**, *19*, 2302925.
- [150] J. Xue, Z. Liu, Y. Fan, R. Wang, Y. Li, *Chem. Eng. J.* **2023**, *476*, 146502.
- [151] K. Srinivas, H. Yu, Z. Chen, A. Chen, M.-Q. Zhu, Y. Chen, *J. Mater. Chem. A* **2024**, DOI: 10.1039/d4ta02444c.
- [152] M.-Y. Yu, Y.-F. Yao, K. Fang, L.-S. Chen, L.-P. Si, H.-Y. Liu, *ACS Appl. Mater. Interfaces* **2024**, *16*, 16132–16144.
- [153] Y. Xiong, Z. Jiang, L. Gong, X. Tian, C. Song, T. Maiyalagan, Z.-J. Jiang, *J. Colloid Interface Sci.* **2023**, *649*, 36–48.
- [154] R. Paudel, U. N. Pan, R. B. Ghising, M. R. Kandel, S. Prabhakaran, D. H. Kim, N. H. Kim, J. H. Lee, *Appl. Catal. B* **2023**, *331*, 122711.
- [155] S.-Q. Deng, Z. Zhuang, C.-A. Zhou, H. Zheng, S.-R. Zheng, W. Yan, J. Zhang, *J. Colloid Interface Sci.* **2023**, *641*, 265–276.
- [156] Y. Sun, Y. Li, S. You, X. Li, Y. Zhang, Z. Cai, M. Liu, N. Ren, J. Zou, *Chem. Eng. J.* **2021**, *424*, 130460.

Manuscript received: June 20, 2024
Revised manuscript received: August 13, 2024
Accepted manuscript online: August 15, 2024
Version of record online: October 17, 2024